Development of material models for semi-brittle materials like tungsten carbide

John F. Moxnes, Jan Arild Teland, Stian Skriudalen, Svein Morten Bergsrud,
Lasse Sundem-Eriksen and Haakon Fykse

Norwegian Defence Research Establishment (FFI)

9 november 2010

FFI-rapport 2010/02225

1120, 1096

P: ISBN 978-82-464-1830-8
E: ISBN 978-82-464-1831-5

Keywords

Wolfram-karbid

Sprekkdannelse

Materialmodell

Numerisk simulering

Perforasjon

Approved by

Eirik Svinsås	Project Manager
Jan Ivar Botnan	Director

English summary

Tungsten carbide is a very special material that exhibits both brittle and ductile properties. While purely brittle and ductile materials in general are well understood, a theory for describing the properties of a hybrid material like tungsten carbide has been elusive. Since this material is often used as the core in projectiles, a better understanding is necessary in order to either optimize the penetration or fragmentation capability or to create optimal protection.

The fragmentation properties of a tungsten carbide projectile was studied systematically by doing perforation experiments with different yaw angles. Then numerical simulations of the experiments were performed, in which the tungsten carbide projectile was modelled using three different materials models, including Johnson-Cook and Johnson-Holmquist. The results showed that none of the models were able to reproduce the experimental results.

To improve on this situation, a new material model (MTSB) based on theory for growth of microcracks was developed. In addition, the Johnson-Cook model was modified with a new dynamic dependency. Numerical simulations of the yaw experiments using the new models showed good agreement with experiments.

MTSB and Modified Johnson-Cook were then put to another test. Oblique impact experiments with tungsten carbide projectile against different steel targets were performed. Numerical simulation of these experiments with both the new material models showed good agreement, in particular for the MTSB. Our conclusion is that both the new models are candidates for being an accurate description of tungsten carbide.

Norwegian summary

Wolfram-karbid er et svært spesielt materiale som har både sprø og duktile egenskaper. Mens rene sprø og duktile materialer generelt er brukbart forstått, har det inntil nå ikke eksistert noen teori for å beskrive egenskapene til wolfram-karbid. Siden dette materialet ofte brukes som hardkjerne i prosjektiler er det nødvendig med en økt forståelse for å kunne optimalisere penetrasjonsevnen og fragmenteringsgraden eller å lage optimal beskyttelse.

I dette arbeidet ble fragmenteringsegenskapene til prosjektiler av wolfram-karbid studert systematisk ved penetrasjonsforsøk med forskjellig yaw-vinkel. Deretter ble det gjennomført numeriske simuleringer av yaw-eksperimentene. Wolfram-karbid prosjektilet ble modellert med tre forskjellige materialmodeller, inkludert Johnson-Cook og Johnson-Holmquist. Det viste seg at ingen av disse modellene var i stand til å reprodusere de eksperimentelle resultatene.

For å forbedre situasjonen ble det utviklet en helt ny materialmodell (MTSB) basert på mikrosprekkteori, samtidig som Johnson-Cook modellen ble modifisert med en ny dynamisk avhengighet. Begge de nye modellene gav godt samsvar med yaw-eksperimentene under numeriske simuleringer.

MTSB og Modifisert Johnson-Cook ble deretter satt på enda en prøve. Det ble gjort eksperimenter med skrått anslag av wolfram-karbid prosjektiler mot plater av forskjellig stålkvalitet. Numeriske simuleringer med begge de nye modellene viste igjen godt samsvar med testene, særlig for MTSB-modellen. Følgelig er begge modellene mulige kandidater for å være en riktig beskrivelse av wolfram-karbid.

Contents

1 Introduction

The analysis of brittle materials subjected to large strains, high strain rates and high pressure is of significant interest due to their extensive use in armor applications, including for personnel, light vehicles and heavy tanks. Much effort has therefore been directed at understanding and modelling brittle materials subjected to impact conditions.

Further, semi-brittle materials with very small grain sizes (down to the nanoscale) are known to have peculiar material properties that might possibly enhance their penetration capability and fracturing behaviour. A lot of research is therefore being performed worldwide on how to best take advantage of this, an important component being the development of accurate material models for semi-brittle materials.

One material of particular interest is tungsten carbide, which is very special since it exhibits both ductile and brittle properties. The particular tungsten carbide studied in this report consists of approximately 10% cobalt and is significantly more ductile than ceramics, while still being very hard.

Generally, because of the high density and hardness, tungsten carbide projectiles have excellent penetration capabilities in steel armor and are therefore often used as penetrators. However, under certain circumstances, such projectiles have been known to fracture early in the penetration process, thus strongly reducing the penetration depth.

In some cases, if the target is relatively thin, fragmentation of the penetrator is actually desirable, as the fragments can cause more damage behind the target than an intact projectile. However, for a thick target, fragmentation can stop the projectile from perforating.

Thus, there is a conflict between the required penetration and fragmentation properties, strongly dependent on the target. Determining an optimal balance is a very difficult problem for the attacker. Similarly, for the defender, it is necessary to know the capabilities of a given armor for stopping tungsten carbide projectiles in order to most efficiently achieve the required protection.

From a practical point of view, designing the most efficient protection or weapon through experimental tests only, can be both expensive and time-consuming. Numerical simulations can help in this regard, but for this to be feasible, an accurate material model for tungsten carbide is necessary. While ductile and brittle materials have been successfully modelled individually, so far an accurate mathematical description of tungsten carbide and similar materials have been elusive. The scope of this report is to improve on this situation.

Earlier work has shown that for yawed impact, the tungsten carbide penetrator is more likely to fracture. We will therefore begin our study by performing systematic yaw experiments to examine this in more detail. Our next step will be to investigate how conventional material

models perform when applied to tungsten carbide under yawed impact. Learning from this, we will look for ways to improve the material models.

2 Ballistic perforation tests with yaw

Our idea was to design an experimental set-up for performing controlled perforation tests with a given yaw, using a projectile with a tungsten carbide core. By varying the yaw angle, the fragmentation pattern as a function of yaw could be revealed.

The projectile which was used in the experiments is shown in Figure 2.1. It is a 7.62 x 51 mm Carl Gustaf AP projectile produced by Bofors.

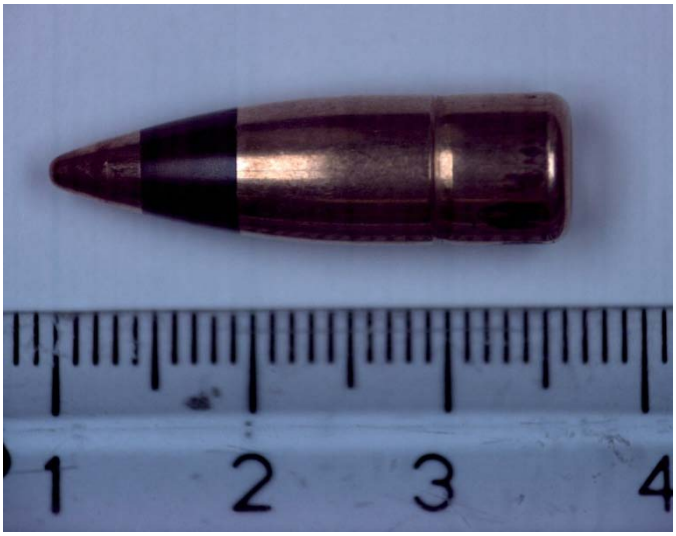

Figure 2.1 7.62 x 51 mm Carl Gustaf AP projectile with tungsten carbide core

2.1 Yaw inducer

Ideally, a projectile will have zero yaw after exiting the gun barrel. To artificially create yaw for the projectile, a device called a "yaw inducer" (shown in Figure 2.2) is fixed at the end of the gun barrel.

The half-barrel configuration of the yaw inducer creates an asymmetry in the force on the projectile, since the gas is only able to flow around on one side of the projectile after escaping the gun barrel. This asymmetry leads to the projectile obtaining yaw. By varying the distance between the gun and the target, the desired yaw angle on impact of the target can be achieved.

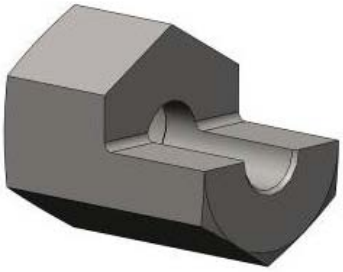

Figure 2.2 Drawing of yaw inducer used in ballistic tests. The extended half barrel measures 20 mm.

In our case the length of the half barrel was 20 mm. The relationship between target distance and yaw angle was found empirically in separate tests using yaw cards, with the results being shown in Figure 2.3. This graph makes it easy for us to obtain a desired yaw angle, just by putting the target at a given
distance.

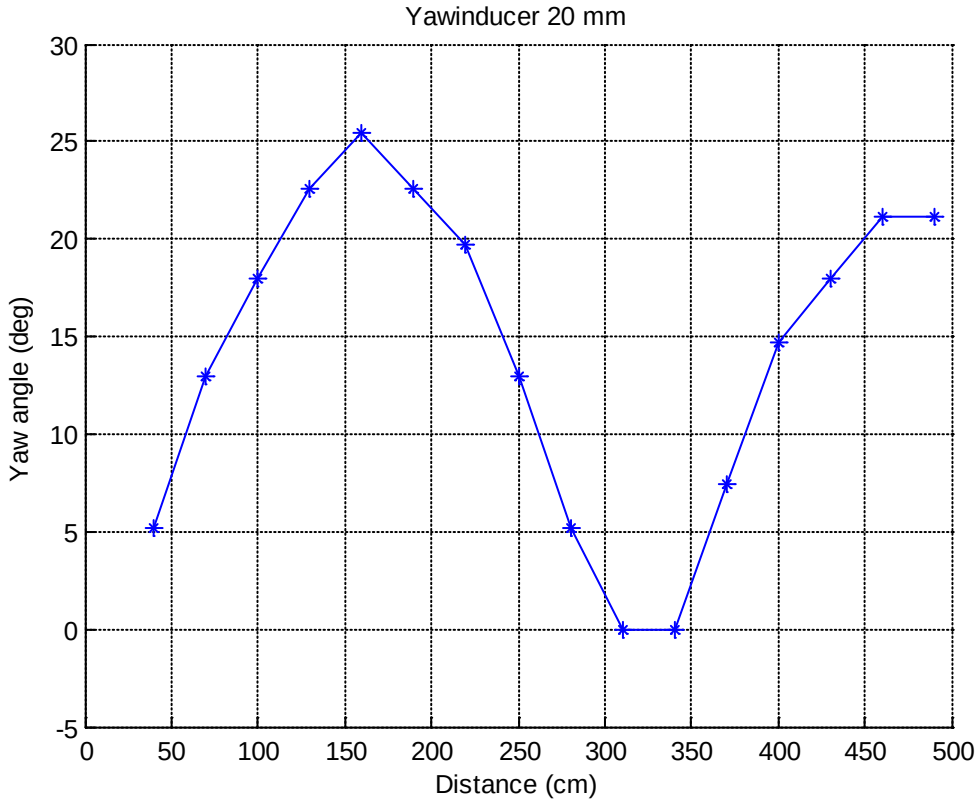

Figure 2.3 Relationship between projectile yaw angle and distance between gun and target for a 20 mm yaw inducer.

2.2 Test setup and description

The test setup for the yaw experiments is shown schematically in Figure 2.4. A standard ballistic test gun was used. Projectile velocity was measured just before target impact. X-ray photography and high speed camera were used to qualitatively assess the behaviour and fracture state of the tungsten carbide after perforation. The distances d_2 and d_3 were approximately 25 cm and 50 cm respectively.

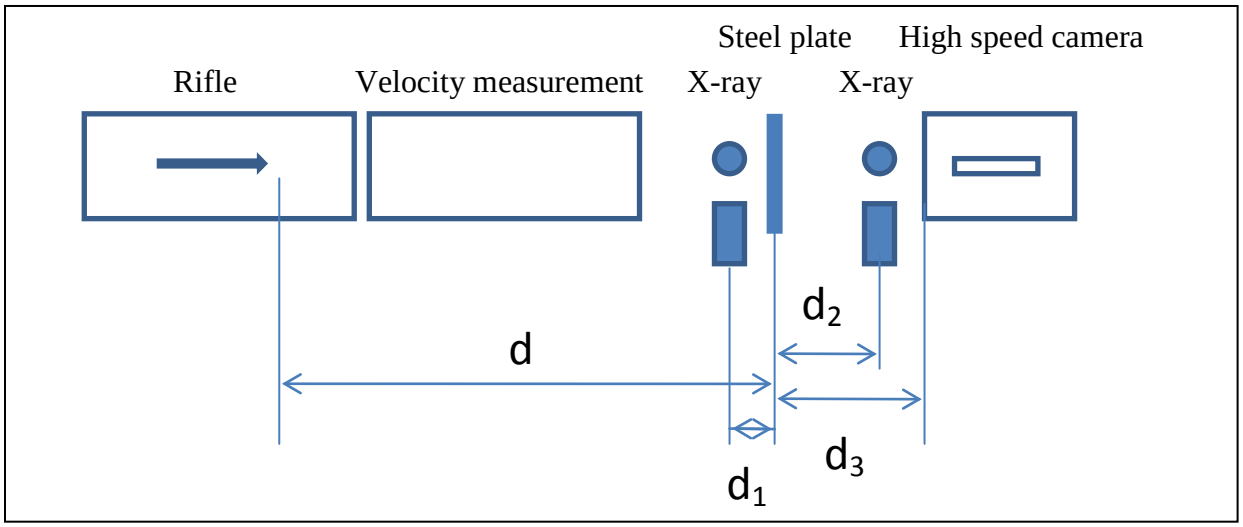

Figure 2.4 Perforation test setup.

Instead of a looking at a continuity of yaw angles, the experiments aimed at studying three separate ranges of yaw angles:

- Small yaw angles (0-4° degrees)
- Intermediate yaw (7-9° degrees)
- Large yaw (18-20° degrees)

The pitch (θ) and yaw (φ) angles of the projectile were measured using X-ray photographies from different angles, no more than 15 cm (d_1) before the steel plate. The total yaw angles[1] (ψ) were then calculated from Equation (2.1)

$$\psi = \arctan\left(\sqrt{\tan^2(\theta) + \tan^2(\phi)}\right) \tag{2.1}$$

As target, 200 mm x 200 mm x 5 mm RHA plates (believed to be roughly similar to Armox 370 although slightly softer) were used. The hardness (Rockwell C) of the RHA plates was measured using an in-house Wizhard hardness testing machine and was found to be 38.4 HRC (361.1 HB) for the plate used in shots 1-16 and 37.7 HRC (358.6 HB) for the plate used in shots 17-27. These hardness values are typical of standard RHA. More details of the hardness measurements are given in Appendix A.

[1] From now on "yaw" will mean "total yaw"

2.3 Experimental results

The actual measured yaw angles in the perforation experiments are shown in Figure 2.5 for each successful shot. In shots number 6, 10 and 17 no x-ray was taken from either one or both sides, making determination of the yaw angle impossible. Also shots 10-13 are disregarded due to misalignment prior to yaw measurements. None of these tests are therefore included in the figure below.

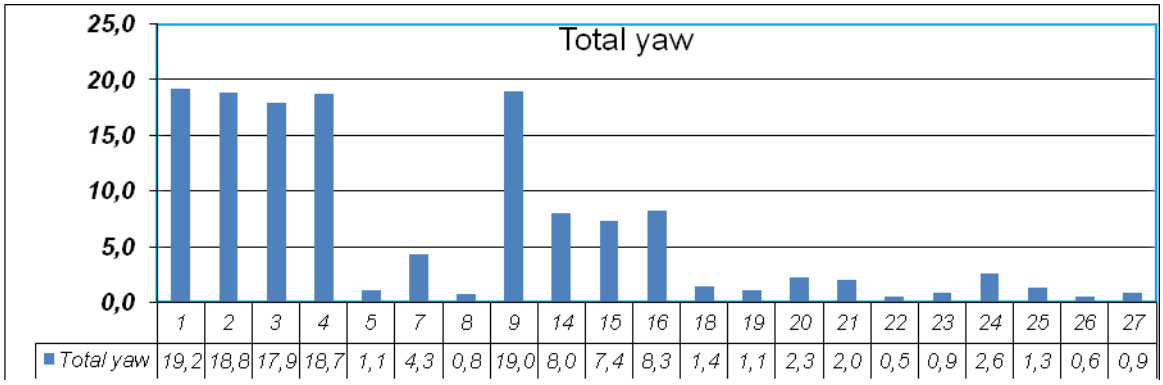

	1	2	3	4	5	7	8	9	14	15	16	18	19	20	21	22	23	24	25	26	27
Total yaw	19,2	18,8	17,9	18,7	1,1	4,3	0,8	19,0	8,0	7,4	8,3	1,4	1,1	2,3	2,0	0,5	0,9	2,6	1,3	0,6	0,9

Figure 2.5 The calculated total yaw angles for the various shots.

The state of the projectile after perforation are shown in Figures 2.6-2.8.

2.3.1 Small yaw angles (0-4 °)

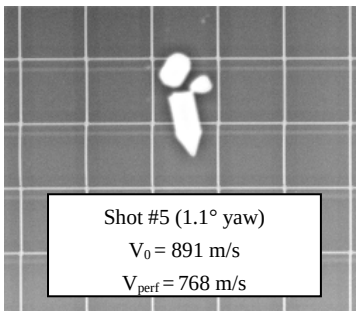

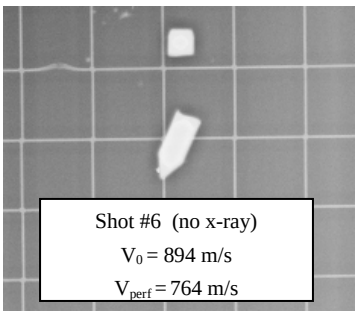

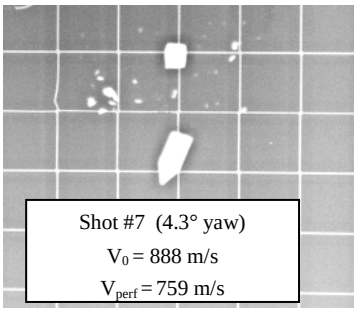

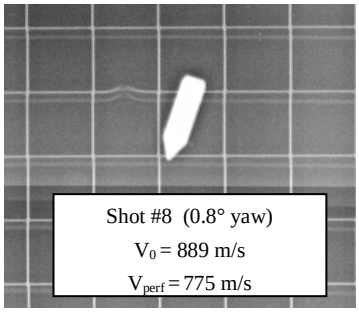

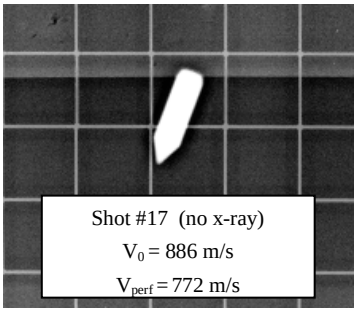

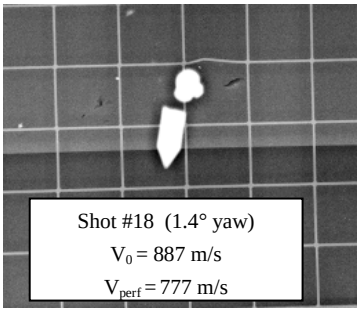

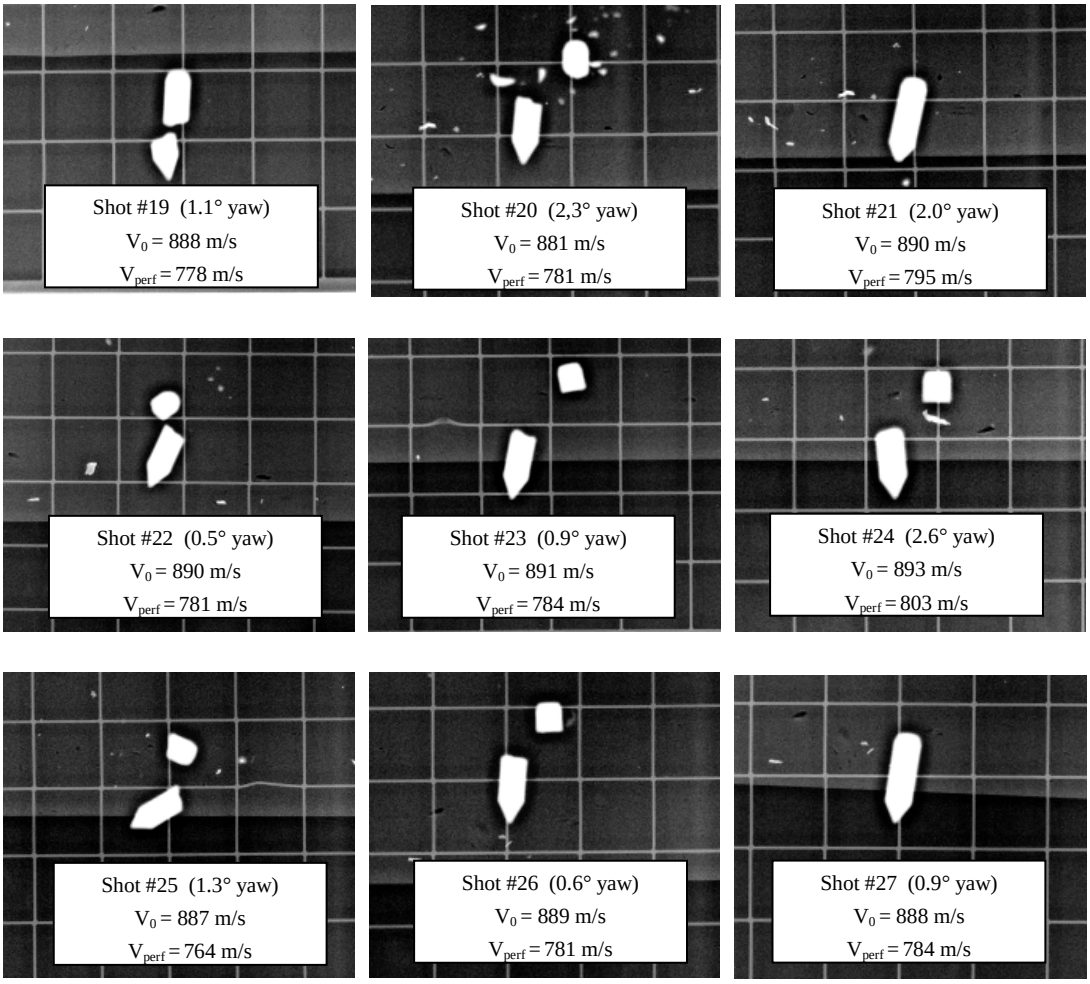

Figure 2.6 X-ray photos after perforation of the RHA plate for small yaw angles.

2.3.2 Intermediate yaw angles (7-9 °)

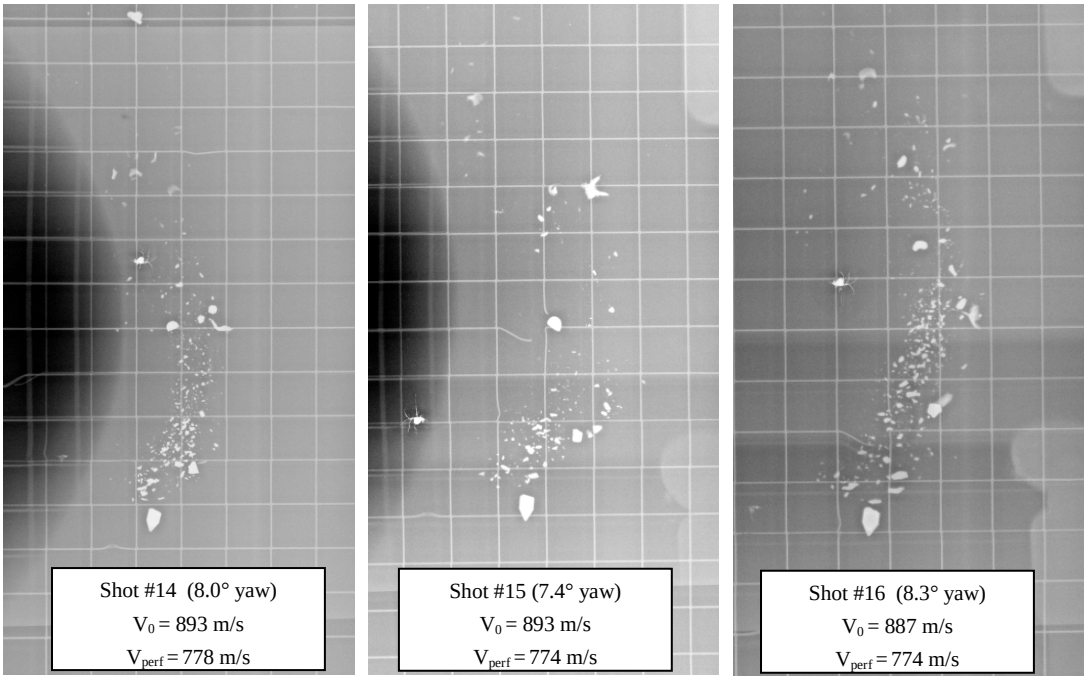

Figure 2.7 X-ray photos after perforation of the RHA plate for intermediate yaw angles.

2.3.3 Large yaw angles (17-19°)

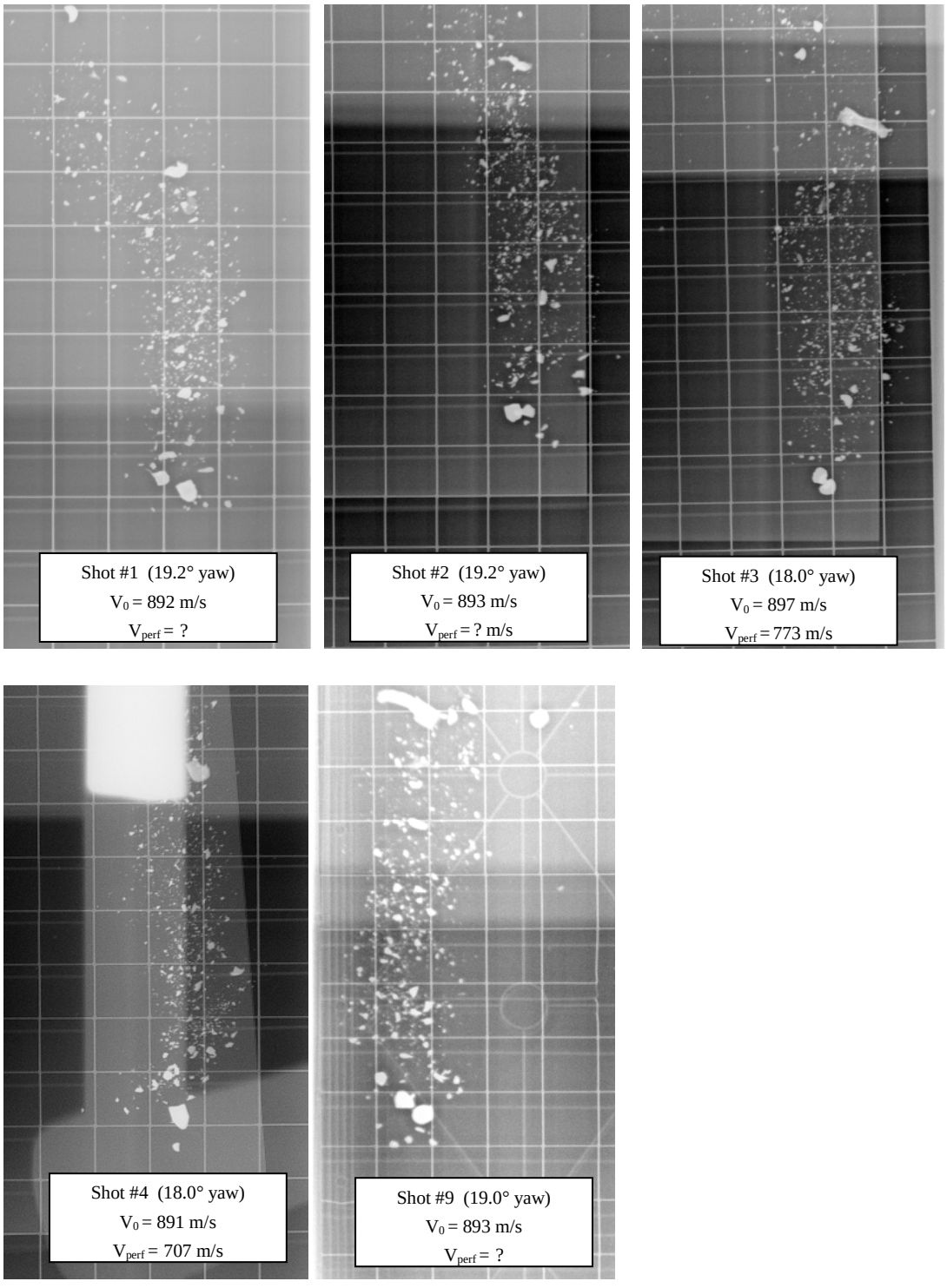

Figure 2.8 X-ray photos after perforation of the RHA plate for large yaw angles. (In shot #4, unfortunately, the clamp holding the steel plate is partly covering the exit of the remaining of the projectile. In shot #9 the circles and large grating is due to the x-ray cassette being put upside down.)

From the x-ray photos we see that for yaw angles close to zero, the penetrator either does not fracture or breaks up into two larger fragments. The fracture surface is typically a little behind the middle of the projectile, i.e. slighly closer to the rear than the front.
The fact that we experience fracture in some cases and not in other similar cases is probably due to some stochastic variation in the material properties of the various penetrators. This is consistent with earlier material tests of tungsten carbide in compression and tension (1-3). It seems clear that small yaw angles is a ”limiting case” where the projectile either fractures or is very close to fracture.

For intermediate yaw angles, we note that the projectile nose is intact whereas the middle of the projectile has broken into relatively small fragments, except for one larger fragment which appears to be the rear end of the projectile.

For large yaw angles the situation is similar to intermediate yaw angles. The nose is mostly intact, although it may have been eroded a little bit. The rest of the projectile is pulverised into very tiny particles, perhaps with a larger fragment at the rear.

The question is now whether the characteristics of these experiments can be reproduced numerically. For this to happen, we first need to find an appropriate material model for tungsten carbide to be used as input to the numerical simulations.

3 Material data from static tests

To determine the properties of our tungsten carbide, the following static tests were performed:

- Uniaxial compression
- Uniaxial tension (actually a bending test, but this can be directly related to tension)

A sketch of the compression test is shown in Figure 3.1. A tungsten carbide specimen fitted with strain gauges is loaded until failure. The tests are described in detail in (1-5). The following discussion of the test assumes some familiarity with elasticicty and plasticity theory. For a good introduction to these topics, see (6,7).

In the elastic regime, the relationship between stress and strain is linear according to Hooke’s law. This makes it particularly simple to derive the elastic constants of the tungsten carbide. For instance (using polar coordinates), the Young’s modulus and Poisson ratio are given by:

$$E = \frac{\varepsilon_{zz}}{\sigma_{zz}}$$

$$\upsilon = -\frac{\varepsilon_{rr}}{\varepsilon_{zz}}$$

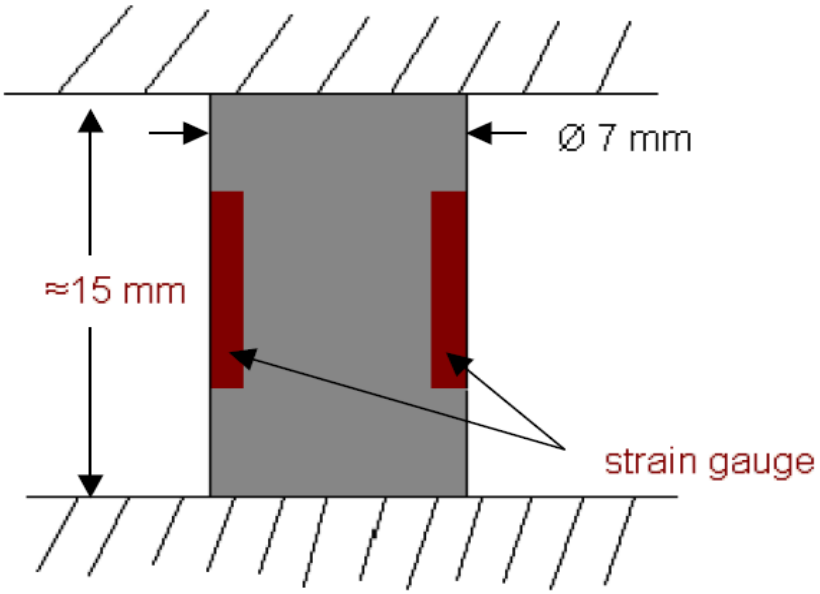

Figure 3.1 Sketch of the uniaxial compression test

As we keep loading the specimen, we find that the stress-strain curve gradually diverges from linearity. This means that the material has reached the yield limit *Y* and plasticity has set in. However, the transition from elasticity to plasticity is not abrupt, so it is customary to define the initial yield limit $Y(\varepsilon_p = 0)$ as the point when the stress-strain curve diverges 2% from linearity.

After yielding, the material no longer obeys Hooke's law. Instead it deformes plastically under the condition $\sigma_M = Y(\varepsilon_p)$. In a uniaxial situation the Mises stress σ_M is equal to $|\sigma_{zz}|$, which enables us to easily determine the yield stress as a function of plastic strain, just by measuring σ_{zz}. For an ideal elastic-plastic material, the yield stress would have remained constant $Y(\varepsilon_p) = Y(0)$ during plastic loading, but it turns out that our tungsten carbide hardens considerably. It should be mentioned here that during the tension test, the yield curve was seen to differ slightly from the one derived during the compression test. However, for now, we ignore this difference.

During loading we can also determine the Equation of State (EOS) of the material by recording the pressure *p* and the total volumetric strain $\varepsilon_V = \varepsilon_{rr} + \varepsilon_{\theta\theta} + \varepsilon_{zz}$. There turns out to be only a small deviation from linearity during plastic loading, which we ignore for now. The EOS is therefore given by the elastic constants. It should be mentioned that according to (8,9), the tungsten carbide EOS shows some non-linearity at very high pressures, but for now we do not account for this effect.

The loading of the test specimen is continued until fracture occurs and the stress (σ_c) and strain (ε_c) at fracture is recorded. This is also done in tension to reveal σ_t and ε_t.
A summary of the material properties derived from these static tests are shown in Figure 3.2 and Table 3.1.

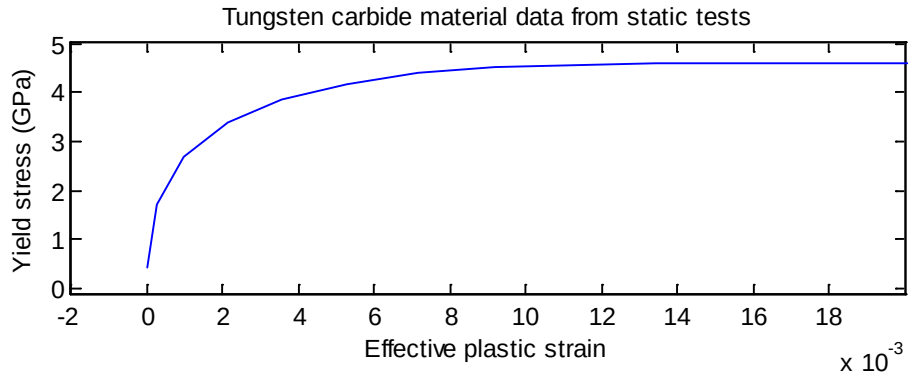

Figure 3.2 Tungsten carbide data yield stress data from static tests

Table 3.1 Tungsten carbide material data

Young's modulus (E)	539 GPa
Poisson ratio (v)	0.23
Initial yield strength Y(0)	0.42 GPa
Compressive strength (σ_c)	4.53 GPa
Tensile strength (σ_t)	3.85 GPa
Compressive plastic strain at fracture (ε_c)	0.0094
Tensile plastic strain at fracture (ε_t)	0.0035

Note that these material properties were derived from a static test and some materials are known to exhibit different properties if loaded dynamically. This will turn out to be crucial in our search for an accurate tungsten carbide material model and will be investigated later on.

4 Material models

Having performed material tests to obtain material parameters for tungsten carbide, we now need to use these within the framework of a material model. As we shall see, this is not as simple as it may seem. Several different material models for brittle materials have already been developed and described in the literature. Typically these models involve the following components:

- Elastic moduli
- Equation of state (EOS)
- Yield stress (possibly as a function of some parameter, like plastic strain)
- Fracture criterion for intact material
- Relationship describing the evolution of the fracture process to complete damage
- Material properties (yield stress etc) for a completely damaged material.

We note that from our static tests we already have data for the three first components listed above. The challenge is therefore the fracture behaviour. This is often referred to as the failure model or fracture model. It may seem that we already have the required information as we have found both the stress and strain at failure in compression and tension. However, this was for a static uniaxial test and there may have been things going on "behind the scenes", which we don't yet know about, and which may be of importance in a dynamic scenario like penetration. It is

therefore not obvious that the fracture criterion is just the few numbers derived from the static test.

Typical brittle materials (glass, ceramics etc) do not accumulate plastic strain before fracture, in which case the fracture criterion is typically a critical combination of stresses. The Johnson-Holmquist fracture models are often applied to such brittle materials.

In contrast, most ductile materials (steel, aluminium etc) accumulate plastic strain before fracture. For these materials the fracture criterion is most easily described by a critical plastic strain, possibly varying with the stress situation. The Johnson-Cook fracture model is often used for ductile materials.

Tungsten carbide is more like a hybrid between ductile and brittle materials since around 2% of plastic strain is accumulated before fracture, and it is therefore not obvious at all what kind of fracture models are appropriate. We will therefore try several different alternatives to see which best fits all the experimental data.

4.1 Simple fracture model

Having just argued that the tungsten carbide fracture model may not be as simple as just using the data derived in the static test, it does not hurt to see whether such an approach could actually work. Our first attempt is therefore called the ”Simple fracture model”. Actually, this is not a model which has been described in the literature. However, it has the obvious advantage of being very simple while in complete agreement with the static material tests. If the perforation experiments can be successfully modelled using a simple fracture model, there is no need for more complex models.

According to the “Simple fracture model”, the yield strength Y may be written as follows:

$$Y = \begin{cases} Y_0(\varepsilon_p) & D = 0 \\ 0 & D = 1 \end{cases} \qquad (4.1)$$

where $Y_0(\varepsilon_p)$ is the data measured in the static tests, displayed in Figure 3.2. We have introduced a new variable D called damage, defined as follows:

$$D = \begin{cases} 0 & p_t < p < p_c \\ 1 & (\varepsilon_p > \varepsilon_c \quad and \quad p > p_c) \quad or \quad (\varepsilon_p > \varepsilon_t \quad and \quad p < p_t) \end{cases} \qquad (4.2)$$

where p is the pressure and p_c and p_t are the pressures at fracture in compression and tension, respectively. We see that this model agrees exactly with the material behaviour of tungsten carbide from the static test. It may seem unnecessary to introduce the damage variable in this case, but it will turn out to be useful later for comparison with other material models. The Simple

fracture model is called a "passive" model because the yield stress is unaffected by the damage until full damage (*D=1*) is reached, at which time it falls instantaneously to zero.

4.2 Johnson-Cook model

The Johnson-Cook (JC) fracture model (10) was initially developed for three metals (OFHC copper, Armco iron and 4340 steel). It has recently been recommended model for describing tungsten carbide used in projectiles (11).

The model for the yield stress *Y* in Johnson-Cook can be written in the following way[2]:

$$Y = \begin{cases} (A + B\varepsilon_p^n)(1 + C\ln\dot{\varepsilon}_p^*) & D < 1 \\ 0 & D = 1 \end{cases} \tag{4.3}$$

where ε_p is the effective plastic strain, **Feil! Bokmerke er ikke definert.** $\dot{\varepsilon}_p^* = \dot{\varepsilon}_p \big/ (1.0\mathrm{s}^{-1})$, and *A*, *B*, *C* and *n* are material constants. We note that the JC-model is also "passive" just like the Simple fracture model.

Since all our tungsten carbide data have been derived from static tests, we have no information about the value of the dynamic parameter *C*. For now we therefore put *C=0*, i.e. completely ignore any dynamic effects. The Johnson-Cook yield stress is then a function of only plastic strain, just as we obtained in our static test. We could determine the parameters *A*, *B* and *n* through a curvefitting procedure roughly to our measured curve in Figure 3.2. However, in numerical simulations, a piecewise linear function can be used as input, so we can in effect directly apply the measured values from the static test. Thus, the yield stress in the JC-model turns out to be exactly the same as in the "Simple fracture model".

However, the fracture part of the JC-model is considerably different from the "Simple fracture model". Instead of just using the measured static failure values, things are more complicated. Johnson-Cook uses the "state variable" damage D, which, instead of jumping discontinously from 0 (intact) to 1 (full damage) (as in the Simple fracture model), evolves according to the following differential equation:

$$\dot{D}(t) = \frac{\dot{\varepsilon}_p(t)}{\varepsilon_f(t)}, \quad 0 \le D \le 1, D(t_0) = 0, \tag{4.4}$$

where $\varepsilon_f(t)$ is called the fracture strain , and $\dot{\varepsilon}_p(t)$ is the plastic strain rate. Thus, the damage is closely related to growth in plastic strain, with the fracture strain as a "controlling factor", describing how "easy" it is to increase the damage. If the fracture strain happens to be small, the

[2] Often the Johnson-Cook yield stress is also written with a temperature-dependent term, but we ignore this.

damage can increase rapidly, whereas a large fracture strain leads to a slow rise in damage. In the JC-model, this fracture strain is given by:

$$\varepsilon_f(t) = D_1 + D_2 exp\left(-D_3 \frac{p(t)}{\sigma_M(t)}\right)\left(1 + D_4 \ln \dot{\varepsilon}_p^*(t)\right) \tag{4.5}$$

where D_1, D_2, D_3 and D_4 are material constants.

To apply the Johnson-Cook model to tungsten carbide, we therefore need to relate the damage constants to our static experiments. Since we are still ignoring potential dynamic effects, D_4 is set equal to zero. Further, we believe that during pure tension the tungsten carbide fractures before obtaining any plastic strain, which is only possible for $D_1 = 0$. This leaves only D_2 and D_3 to be determined.

This can be done from our static compression and tension tests. During uniaxial compression and tension, we have $p = \frac{1}{3}\sigma_{zz} = \pm\frac{1}{3}\sigma_M$. Thus, the ratio $\frac{p}{\sigma_M}$ is constant, equal to $\pm\frac{1}{3}$ depending on whether we have compression or tension. (Note that it is only during uniaxial stress that we have this property, which makes such tests so convenient for deriving JC material data).

During uniaxial compression and tension, Equation (4.5) therefore reduces to the following constant fracture strain ε_f^0:

$$\varepsilon_f(t) = \varepsilon_f^0 = D_2 \exp\left(\pm\frac{D_3}{3}\right) \tag{4.6}$$

If we insert this into Equation (4.4) for damage growth, we see that the time dependence vanishes and it can easily be integrated to give damage as an explicit function of plastic strain:

$$D(\varepsilon_p) = \frac{\varepsilon_p}{\varepsilon_f^0} = \frac{\varepsilon_p}{D_2 \exp\left(\pm\frac{D_3}{3}\right)} \tag{4.7}$$

Further, we know that if tungsten carbide is actually described by the Johnson-Cook model, the damage D will be 1 at compressive and tensile failure. Thus, we have the following two conditions:

$$D(\varepsilon_c) = D(\varepsilon_t) = 1$$

which when inserted into Equation (4.7) enables us to easily determine D_2 and D_3 as a function of the compressive and tensile fracture strain:

$$D_2 = \sqrt{\varepsilon_c \varepsilon_t} \qquad D_3 = -\frac{3}{2}\ln\left(\frac{\varepsilon_c}{\varepsilon_t}\right) \tag{4.8}$$

So to sum up: With the assumptions of no dynamic effects and failure in pure tension without plastic strain, all the necessary tungsten carbide Johnson-Cook parameters have been determined from our static uniaxial tests.

4.3 Johnson-Holmquist failure model

The Johnson-Holmquist constitutive model was developed to describe the response of ceramics to large deformations. There are actually two Johnson-Holmquist models (JH-I and JH-II). The JH-I model (12) is a passive model, so the transition from intact to failed strength is instantaneous once a critical damage value is attained. However, in the JH-II model (13), the degradation of strength is incremental: the strength decreases as damage develops. This model is currently widely used to describe ceramics and will therefore be studied here to see whether it can be applied to tungsten carbide. It should be noted, though, that some investigations have found limitations with the JH-II models in the prediction of tensile cracks (14).

The yield stress Y in the JH-model can be written as:

$$\begin{aligned} Y &= \left[A(p^* + T^*)^n (1-D) + B(p^*)^m D\right]\left[1 + C\ln(\dot{\varepsilon}_p^*)\right] \\ p^* &= \frac{p}{p_{HEL}} \qquad T^* = \frac{T}{p_{HEL}} \end{aligned} \tag{4.9}$$

where p_{HEL} is the pressure at the Hugoniot Elastic Limit (HEL), T is the maximum hydrodynamic tensile strength and *A, B,C, n* and *m* are material parameters[3]. The HEL is the yield limit in uniaxial strain, i.e. when a confined material is loaded in one direction, see (7) for more details.

Note that instead of having two separate expressions for the yield stress, when *D=1* or *D<1*, in Johnson-Holmquist the yield stress is a continuous function of damage *D*. Material models with this property are called "active" fracture models. Note that for the special cases D=0 (no damage) and D=1 (full damage), the yield stress reduces to the following:

$$\begin{aligned} Y &= A\left(p^* + T^*\right)^n \left(1 + C\ln(\dot{\varepsilon}_p^*)\right) \qquad \textit{Intact} \qquad (D=0) \\ Y &= B\left(p^*\right)^m \left(1 + C\ln(\dot{\varepsilon}_p^*)\right) \qquad \textit{Fragmented} \quad (D=1) \end{aligned}$$

We also note that the Johnson-Holmquist model differs considerably from Johnson-Cook in other respects. For example, the yield stress depends explicitly on the pressure instead of plastic strain.

[3] Although the same symbols are used for the notation, the parameters are obviously not the same as in the Johnson-Cook model. To distinguish explicitly, we could have used a notation like A^{JC} and A^{JH} etc, but we decided against this to avoid cluttering up the equations with indices.

Unfortunately, we shall see that this means that determining the material constants *A, B, C , n* and *m* will not be as simple as for Johnson-Cook.

The fracture part of the model, i.e. the differential equation for the evolution of damage is similar to Johnson-Cook, but with a different definition of the fracture strain:

$$\dot{D}(t) = \frac{\dot{\varepsilon}_p(t)}{\varepsilon_f(t)}, \quad 0 \le D \le 1, D(t_0) = 0,$$
$$\varepsilon_f(t) = D_1 \left(\frac{p(t)+T}{p_{HEL}} \right)^{D_2} \tag{4.10}$$

where D_1 and D_2 are material constants.

Let us again assume that *C=0*, i.e. no dynamic effects, as for the other fracture models and try to determine *A, B,n* and *m* from the uniaxial compression and tension tests. We then immediately encounter a problem. For JC, the yield stress was a function of plastic strain, and in the uniaxial tests, we could measure the Mises stress, which was equal to the yield stress during plasticity, together with the plastic strain to easily determine the relationship. However, in JH, the yield stress is a function of pressure instead. One might think that it would be a similarly simple task of recording the pressure and Mises stress during the test to develop a relationship, but this is not so. During uniaxial loading, we always have the identity $\sigma_M = 3p$, independent of whether we have elasticity or plasticity. So, if we record the Mises stress and pressure, we learn nothing about the yield stress, except for the maximum value.

Thus, while we are loading the material, after a while it will start flowing plastically and harden (which we would only notice by watching the Mises stress and strain). Damage will grow in the JC-model, but the pressure and Mises stress remain proportional. To develop data for the JH-model, though, we need to "pretend" that the material is still behaving elastically, thus no growth in damage. Thus, while in JC the damage is growing during plastic loading, the damage remains zero in JH. We already see that the JH framework can not be consistent with out static material tests, but let us try to proceed anyway to see what can be derived.

In compressive loading, we eventually reach a maximum value for the pressure p_c and Mises stress $\sigma_{M,c}$ after which they both suddenly falls to zero (because of fracture). In JC, this was the point when damage reached 1. In JH, however, we will assume that this is the point when damage starts growing, thus the intersection with the yield stress curve. The point $(\sigma_{M,c}, p_c)$ is therefore one point on the yield stress curve for *D=0*. Similarly, from a tension test, we obtain another point $(\sigma_{M,t}, p_t)$ on the same curve. For additional points, we would need to do confined tests (5). Two points on the JH yield stress curve is therefore all that is given by the static tests.

But, how can we take the point when the material fractures as the start of increasing damage? This is dubious, but in fact, it could be consistent with the static tests. Due to limitations in the static test equipment, it is conceivable that the plastic strain increased after the fracture strain was reached, but that we just were unable to measure it. Assuming this is actually what happened, it is consistent to take this point as the start of plastic flow.

Anyway, having only two points on the yield curve, there is no end to the amount of possible yield curves, as long as they pass through these points. So with our limited test data, we have a lot of freedom in determining A, T and n. As long as they pass through the two "measured" points, they are consistent with data. Two examples (which we will be using in the numerical simulations later) are illustrated in Figure 4.1.

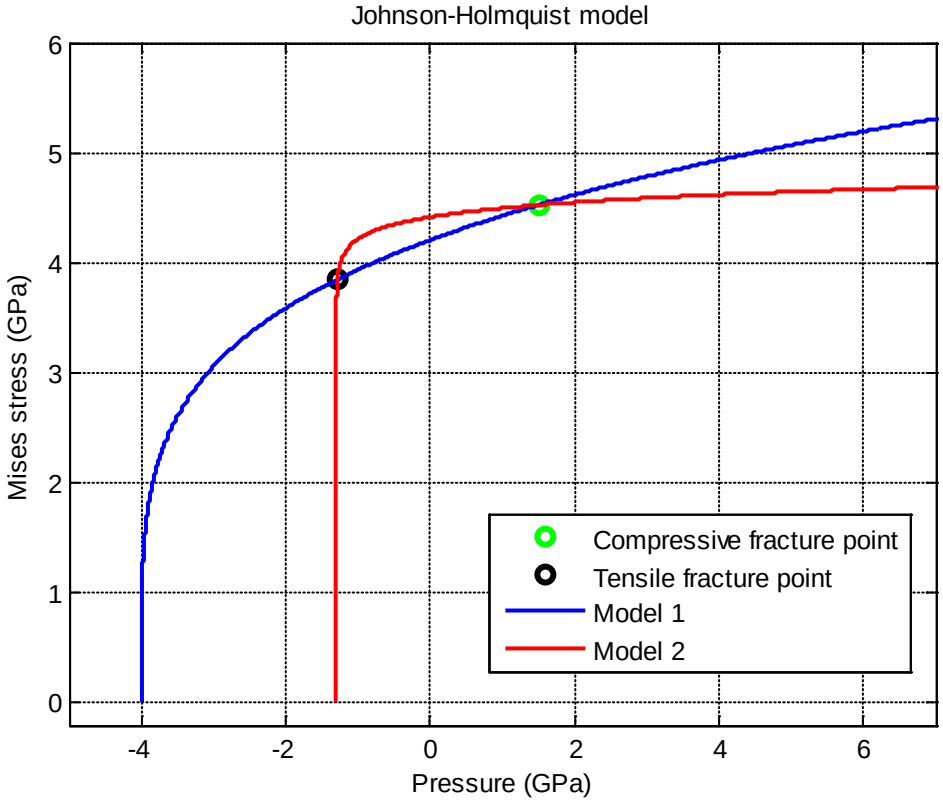

Figure 4.1 Two of many possible (D=0) yield curves for the JH-model, based on the two experimental points which can be found from the static tests.

For the fracture part *(D=1)* of the yield stress curve, we apply the Occam's razor principle[4] and assume that *m=n* so that it has the same shape as the *D=0* curve. Further, we assume that the coefficient *B=A*. Thus, fracture only shifts the curve by the tensile pressure T. This can be seen as an example of the Occam's razor principle, but can also be defended by appealing to a theory that there is a pressure dependent part and one density dependent part of the yield stress curve.

This completes the derivation of the yield stress parameters for Johnson-Holmquist.

[4] This principle is often popularly summarized as "The simplest explanation is more likely the correct one".

In the JH-framework it is also more difficult to extract the fracture parameters D_1 and D_2 from the simple tension and compression experiment. Assume that our uniaxial compression/tension test is described by the JH-model, and that we have reached the yield stress. The material then starts behaving plastically (in reality it has started behaving plastically long before). Putting *C=0* (since the experiment is static), during plasticity and using that $p = \sigma_M / 3$ in uniaxial stress, the following set of equations must now be satisfied:

$$\sigma_M = \left(A\left(\frac{\sigma_M}{3} + T \right)^n (1 - D(\varepsilon_p)) + B\left(\frac{\sigma_M}{3} \right)^m D(\varepsilon_p) \right) \tag{4.11}$$

$$\dot{D}(t) = \frac{\dot{\varepsilon}_p(t)}{\left(D_1\left(\sigma_M / (3\bar{p}) + T / \bar{p}\right)\right)^{D_2}}, \quad 0 \le D \le 1, D(t_0) = 0, \tag{4.12}$$

By inserting Equation (4.11) into (4.12), we can solve for *D* as a function of ε_p. Inserting the solution into Equation (4.11) then gives us an expression for σ_M as a function of ε_p. In practise, the two equations must be solved numerically. In any case, the behaviour during plasticity, as the damage grows from 0 to 1 can, in principle, be determined as a function of the yet undetermined parameters D_1 and D_2.

For JC we determined the corresponding damage parameters from the requirement that damage was equal to 1 when the plastic strain was equal to the compressive/tensile strain. This approach does not work in the JH-model because when damage starts growing, the plastic strain is already equal to the compressive/tensile strain! (Due to our assumption that there is no plastic strain hardening, and that the plastic strain grows larger than the compressive/tensile strain, but that we were unable to measure it).

Therefore we need another condition to determine D_1 and D_2 for tungsten carbide described using the JH-model. We choose the condition that the deformation energy in the static tests (compression and tension) described (incorrectly) using the JH-model should be equal to the actual measured deformation energy. Mathematically, this gives us the two necessary equations to determine the damage constants:

$$\begin{aligned} \int_0^{\varepsilon_c^{JH}} \sigma_M^{JH} d\varepsilon^{JH} &= \int_0^{\varepsilon_c^{\exp}} \sigma_M^{\exp} d\varepsilon^{\exp} \\ \int_0^{\varepsilon_t^{JH}} \sigma_M^{JH} d\varepsilon^{JH} &= \int_0^{\varepsilon_t^{\exp}} \sigma_M^{\exp} d\varepsilon^{\exp} \end{aligned} \tag{4.13}$$

This is further illustrated in Figure 4.2. We see that the lack of strain hardening in the JH-model makes it impossible to agree exactly with the experimental results, but we approximate by

assuming a similar deformation energy. For ceramic materials, where JH has been applied successfully, there is usually no strain hardening and therefore better agreement with experiment.

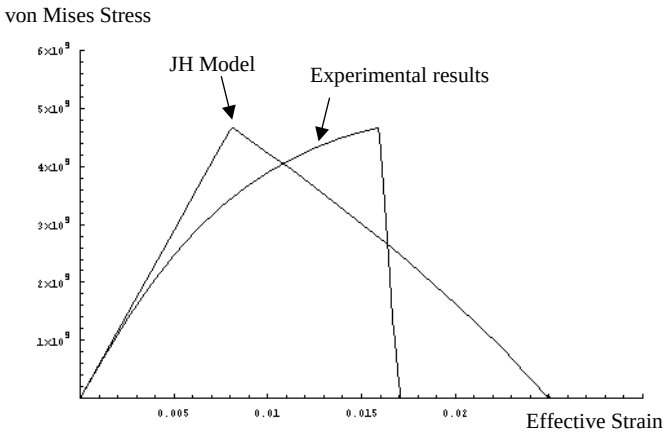

Figure 4.2 *Mises stress as a function of strain during simple compression in the* JH-model *and experimentally. To determine the damage constants D_1 and D_2, the area under the curves is assumed equal.*

To sum up: The Johnson-Holmquist framework is not consistent with the results from our static tests. Nevertheless, by making a range of assumptions we were able to derive data for all the required material parameters.

4.4 Summary of material models

In this chapter we have derived tungsten carbide parameters for three very different material models. In Table 4.1 an overview of these models is given.

Table 4.1 Summary of material models

	Simple	Johnson-Cook	Johnson-Holmquist II
Type	Passive	Passive	Active
Fracture parameter	Damage	Damage	Damage
Dynamic effects	None	Yield function Failure strain	Yield function
Stress or strain based	Stress and strain	Strain	Stress

5 Numerical simulations

In the previous chapter we derived tungsten carbide data for three different material models. We will now perform numerical simulations with these three models to see whether they are able to reproduce the experimental results from the yaw experiments. In this way we can check whether the material models are correct, or more precisely, we can check whether some of them are wrong and rule them out as candidates for describing tungsten carbide.

All simulations were performed in 3D using ANSYS AUTODYN 12.0. The projectile was modelled in Lagrange using an unstructured grid. The geometry was imported from a CAD-drawing and the mesh was generated using the standard settings in ANSYS Workbench (15). Only the tungsten carbide core was modelled. Impact velocity was chosen to be 890 m/s. For yaw angles we used 0, 8 and 18 degrees.

The target was modelled using the Euler multimaterial solver. The grid was graded, with the element size being 0.5 mm in the part where the projectile impacted and larger cells further out. It would also have been possible to model the target using Lagrange, but this would have meant applying numerical erosion of the target in order to remove highly deformed cells. Also, earlier work (14,15) has shown that Lagrange-Lagrange is not suitable for modelling impact simulations with brittle materials because of the presence of unphysical stress spikes. The RHA material model was taken from (14) and is reproduced in Appendix B. In Figure 5.1 the simulation set-up is illustrated for zero degrees yaw.

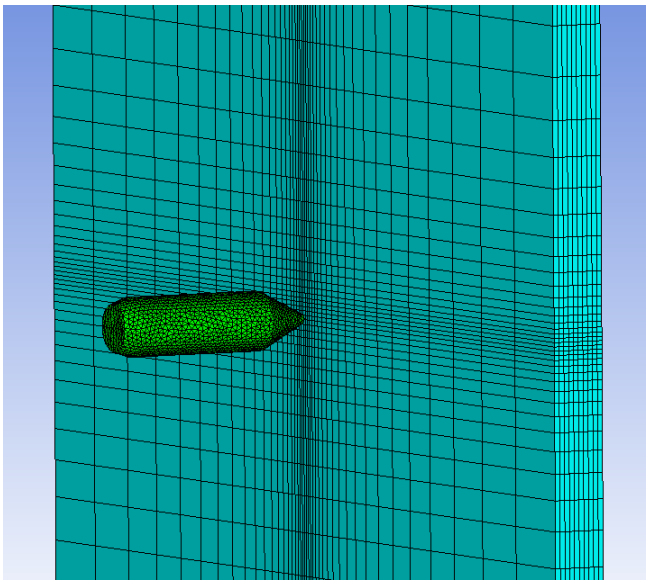

Figure 5.1 Set-up up of the numerical simulation (zero yaw).

5.1 To erode or not erode – that is the question

Since the projectile is modelled in Lagrange, we face a potential problem in cases where the projectile fractures. A fractured cell will lose strength and can thereafter be easily deformed.

This will create numerical problems with grid entanglement if the cell becomes too distorted, a classic problem in numerical modelling.

To avoid this, distorted cells are often removed artificially by a given criteria. This process is called numerical erosion and is often necessary for the simulation to run. Since this is not a physical process, one has to be careful in choosing an appropriate erosion criteria that does not influence the physical solution too much.

One possibility would be to erode all fractured cells. This would have the advantage of quickly getting rid of problematic cells and it would be easy visualize the cracks. It could also be argued that this is physically correct since in reality the fractured cells would lose contact with the intact projectile and not interact with it.

Another option is to keep the failed cells and use another erosion criteria so that only very distorted cells are removed (strain equal to 2.0 is usually a safe choice). This should be "safer" since only very few cells will be eroded. A drawback is the visualization, which may look odd with some cells being very deformed and protruding from the projectile body. This can be fixed by using the "Fragment plot" option in AUTODYN, which means that the failed cells are not plotted, even though they are present in the simulation. Since this fixes the visualization problem, while still being "safe", this will be our method of choice.

We will now present the simulation results of the yaw experiments for the various fracture models. The state of the projectile after perforation of the target (at T=4.0 ms after impact) will be shown and it is to be hoped that it will look similar to the x-ray photos in Figures 2.6-2.8. Note that there will be no "debris cloud" in the simulations plots since failed cells are hidden from view.

Simple fracture model

The simple fracture model is not standard in AUTODYN but was implemented through a user subroutine. The material parameters were taken directly from Table 3.1. Results are shown in Figure 5.2. In general, the agreement with experiments is poor. The nose is never intact and there is no cracking of the middle part of the penetrator.

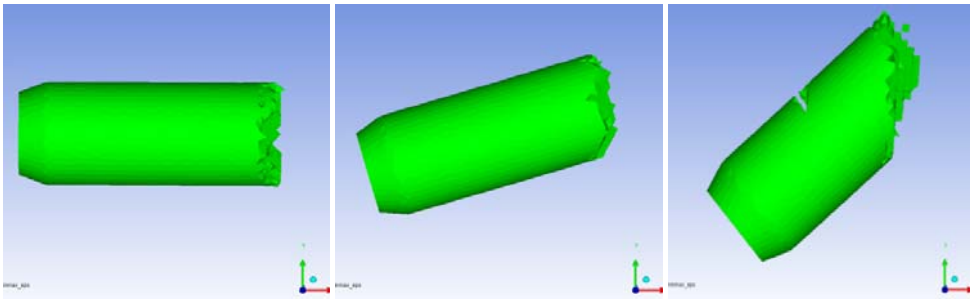

Figure 5.2 State of the projectile after perforation of 5 mm RHA when using the Simple Fracture model. (Left: 0 degrees yaw, Middle: 8 degrees yaw, Right: 18 degrees yaw)

5.2 Johnson-Cook failure model

The JC yield stress parameters were taken from Table 3.1, just as for the Simple fracture model. For our tungsten carbide, the values of D_2 = 0.0057 and D_3 = -1.48 were found for the damage parameters from Equation (4.8).

The results for the Johnson-Cook failure model are given in Figure 5.3.

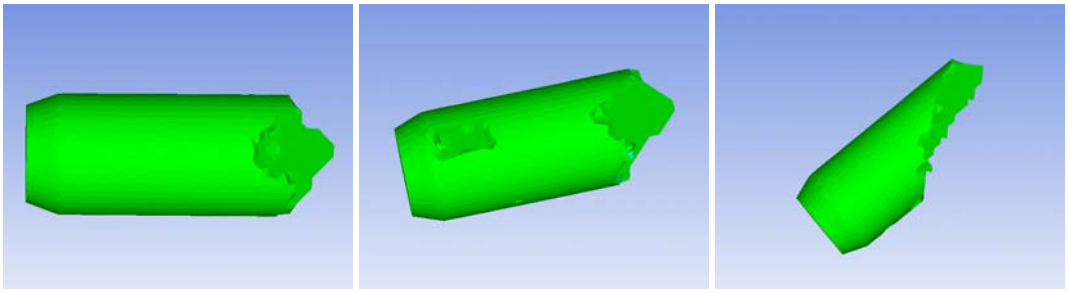

Figure 5.3 State of the projectile after perforation of 5 mm RHA when using the Johnson-Cook model. (Left: 0 degrees yaw, Middle: 8 degrees yaw, Right: 18 degrees yaw)

Also for the JC-model, we note that the simulation results are in poor agreement with the experimental results. Again, the nose does not remain intact unlike in the experiments. Secondly, the middle of the projectile body does not fracture at 8 degrees. There may be some fracture at 18 degrees, but this is difficult to determine since so much of the projectile body has eroded.

5.3 Johnson-Holmquist II

Given all the freedom we have in estimating the JH-parameters, we decided to look at two different sets of parameters, one with a “high” hydrodynamic tensile limit of -4.0 GPa and one with a “low” limit of -1.3 GPa. These are in fact the two models shown in Figure 4.1. The terms “high” and “low” could perhaps create some confusion since tensile stress is negative, but is intended to mean that the high hydro tensile model can withstand a higher hydrostatic tension. The complete list of material parameters used in the JH-simulations are given in Appendix B.

Figures 5.4-5.5 shown the Johnson-Holmquist results for the two different parameter sets.

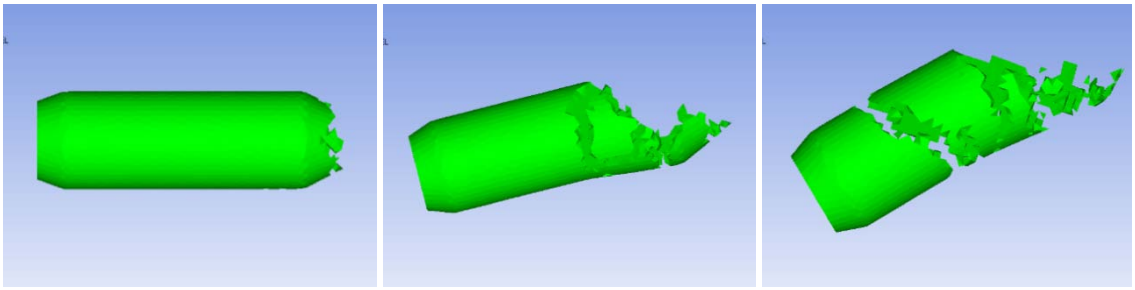

Figure 5.4 State of the projectile after perforation of 5 mm RHA when using the JH-model and a high hydrodynamic tensile limit (-4.0 GPa). (Left: 0 degrees yaw, Middle: 8 degrees yaw, Right: 18 degrees yaw)

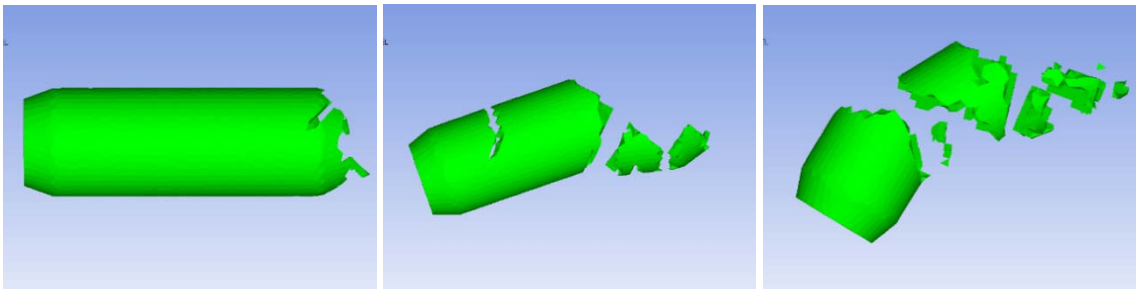

Figure 5.5 State of the projectile after perforation of 5 mm RHA when using the JH-model and a low hydrodynamic tensile limit (-1.3 GPa). (Left: 0 degrees yaw, Middle: 8 degrees yaw, Right: 18 degrees yaw)

Again the agreement is not impressive. The nose is destroyed, which is not correct. However, there are some indications of break-up of the middle of the projectile body, which is good. The fracture pattern does not seem to be very sensitive to the hydrodynamic tensile limit, since both the “high” and “low” model give relatively similar results.

5.4 Summary

In general the numerical results are not very promising. None of the models are able to predict that the projectile nose remains intact. The simple fracture model does not predict fracture in the projectile body for neither 8 or 18 degrees of yaw, although there are some indications of a

growing crack for 18 degrees. The Johnson-Cook model gives similar results, but with even more failed cells. The Johnson-Holmquist model (which can be ruled out as a valid description of tungsten carbide since it is not in agreement with the static experiments) actually provides the best results, managing to fragment the projectile in several parts for 8 and 18 degrees yaw.

6 Dynamic effects

So, what can be done to improve the situation? Clearly our static tests did not reveal all the material data needed to completely describe tungsten carbide. The Simple fracture model and Johnson-Cook model are in complete agreement with these tests, but perform poorly when applied to the yaw experiments. One obvious thing is that dynamic effects have been neglected. Some materials are stronger when they are loaded rapidly (18-22), and tungsten carbide might be one of them.

We saw that both the Johnson-Cook model and the Johnson-Holmquist models contained dynamic terms multiplying the whole yield stress expression. In fact, JC even had two dynamic terms, the other one multiplying the fracture strain. Unfortunately, we have no idea of the value of the dynamic parameters since we have performed no dynamic tests. We will therefore try to determine them indirectly by tuning them until the simulation results are (hopefully) in better agreement with the experiments.

6.1 Johnson-Cook

We first try tuning D_4 in the Johnson-Cook model. Increasing this parameter means that the fracture strain will increase, thus limiting the damage growth and resulting in a stronger projectile. Several simulations were performed, trying to estimate the lowest value of D_4 which resulted in an intact nose. It was found that D_4=0.35 was such a limiting case. This parameter value then gave the results shown in Figure 6.1.

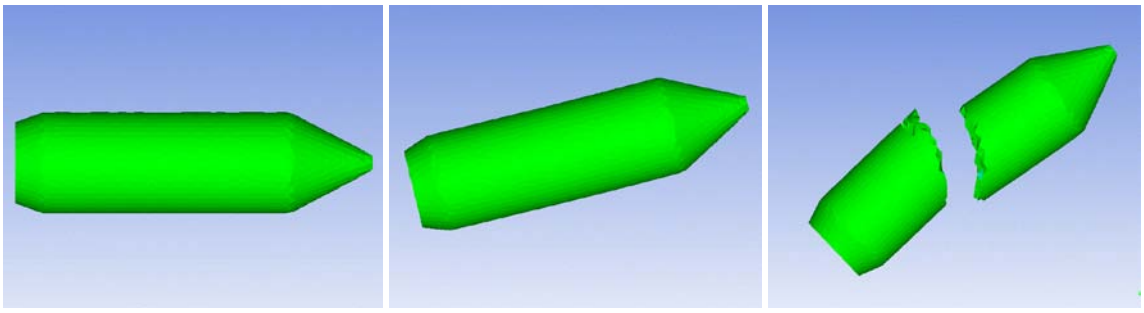

Figure 6.1 State of the projectile after perforation of 5 mm RHA when using the Johnson-Cook model with dynamic effects turned on(D_4=0.35). (Left: 0 degrees yaw, Middle: 8 degrees yaw, Right: 18 degrees yaw)

We see that the nose now remains intact, but so does the body, except at 18 degrees yaw. So, the result seem to have improved slightly, but are still far from being correct. Tuning the parameter C in the yield stress gives similar results.

6.2 Johnson-Holmquist

For Johnson-Holmquist, the dynamic term is only in one position, multiplying the yield stress. By tuning the strain rate parameter to the smallest value that keeps the nose intact, a value of *C=0.09* was found for both Model 1 (high tensile limit) and Model 2 (low tensile timit). The results are shown in Figures 6.2 and 6.3.

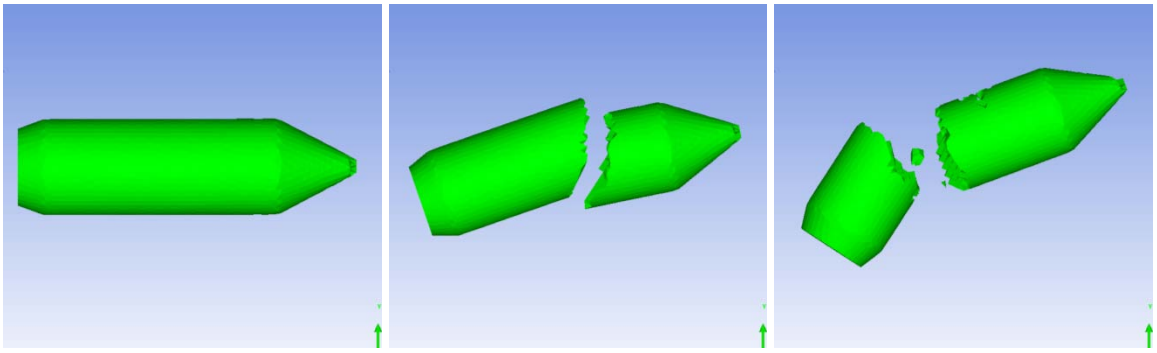

Figure 6.2 State of the projectile after perforation of 5 mm RHA when using the JH-model and a high tensile limit (-4.0 GPa) and with dynamic effects turned on (C=0.09). (Left: 0 degrees yaw, Middle: 8 degrees yaw, Right: 18 degrees yaw)

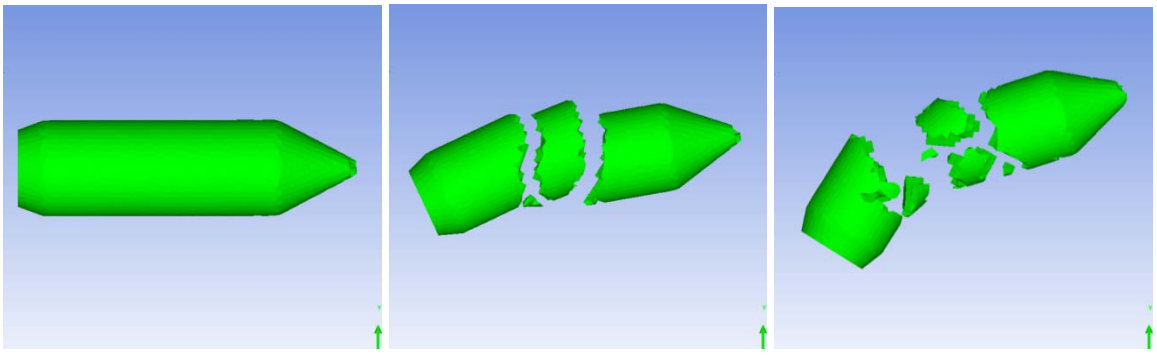

Figure 6.3 State of the projectile after perforation of 5 mm RHA when using the JH-model and a low tensile limit (-1.3 GPa) and with dynamic effects turned on (C=0.09). (Left: 0 degrees yaw, Middle: 8 degrees yaw, Right: 18 degrees yaw)

The Johnson-Holmquist results look quite promising, especially with a low tensile limit. The only problem is that, as mentioned, this material model can not be correct for tungsten carbide since it does not agree with the static tests.

6.3 Summary

It seems that if we include dynamic effects to “save the nose”, the whole projectile body becomes too strong (i.e. not brittle enough). So, although there was some improvement when dynamic effects were included, none of the models seem able to describe the behaviour of tungsten carbide in both the static tests and the yaw experiments. The Simple fracture model and JC agree with the static tests but fail the yaw experiments, and vice versa for the JH-model. A summary of our findings so far is given in Table 6.1.

Table 6.1 Tungsten carbide material models

	Simple	Johnson-Cook	Johnson-Holmquist II
Description			
Type	Passive	Passive	Active
Fracture parameter	Damage	Damage	Damage
Dynamic effects	None	Yield function, fracture strain	Yield function
Stress or strain based	Stress and strain	Strain	Stress
Performance			
Static test	Ok	Ok	Failed
Yaw test	Failed	Failed	Ok
Status	Falsified	Falsified	Falsified

7 New material models

Since all the tungsten carbide fracture models tried so far have all failed, it is necessary to develop new models. The work will proceed along two different lines:

- Developing a new model from scratch based on microcrack growth instead of the damage parameter
- Improving the Johnson-Cook model through a better strain rate dependency

7.1 MTSB crack growth model

A disadvantage with the damage parameter D in the fracture models, is that it can not be measured directly. It would be better to have the model depend on a parameter which could be measured. On a microscale, fracture in brittle materials is related to the growth of microcracks. An example of such a microcrack is shown in Figure 7.1. These cracks nucleate and propagate simultaneously in the material, ultimately merging into macrocracks, separating the solid material into fragments. A correct fracture model should be based on these facts.

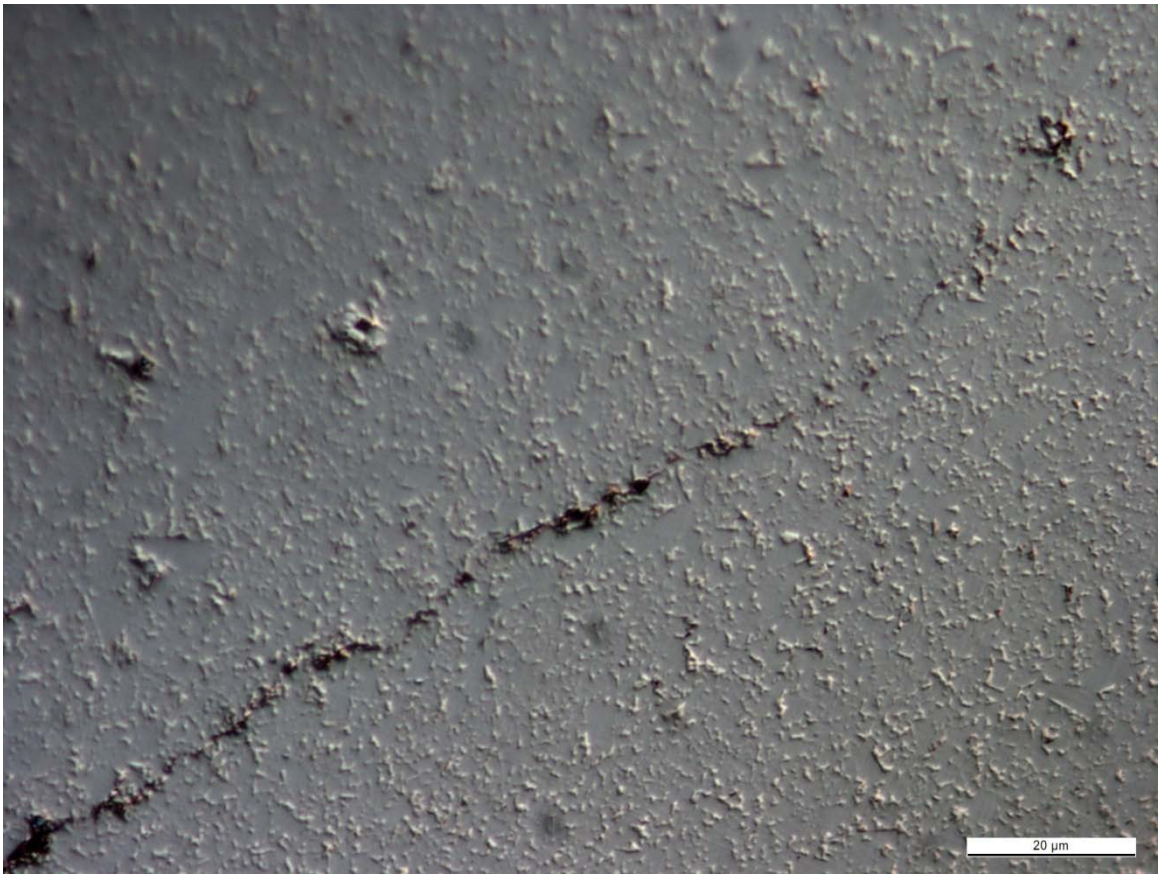

Figure 7.1 Microcrack in tungsten carbide (scale is shown in bottom right corner).

In this chapter we propose a new material model called the MTSB (Moxnes-Teland-Skriudalen-Bergsrud) crack growth model, based on the idea of microcracks. The MTSB model contains two components:

- Theory describing the development of microcracks
- Theory relating the microcrack properties to macroscopic material properties like yield stress.

7.1.1 Microcrack theory

The first thing we need in MTSB is a relationship describing the growth of microcracks, i.e. what causes the microcracks to grow and the speed at which they are growing. This could perhaps be

calculated analytically, using a quantum mechanical model of tungsten carbide. However, this is clearly very difficult and beyond the scope of this report.

Instead we will be guided by our experience with tungsten carbide, while at the same time following the Occam's razor principle of keeping things as simple as possible (until proven wrong).

It does not seem unreasonable that the crack growth is related to the plastic strain rate. Let us initially assume a linear relationship between them. Further, let us assume that the we have a fracture strain parameter which "regulates" the crack growth in a similar way as in Johnson-Cook and Johnson-Holmquist. Thus, we propose for the MTSB model:

$$\frac{\dot{\lambda}(t)}{R_c} \overset{mod}{=} \frac{\dot{\varepsilon}_p(t)}{\varepsilon_f\left(p(t)\right)} \tag{7.1}$$

where λ is the average crack length and R_c is a characteristic dimension of the volume we are studying. We will assume that for reasonable volume sizes (at least ten times larger than the grain structure of the material), the average crack length per unit length is constant for a given damage. This enables us to define a damage parameter D corresponding to the crack length:

$$D(t) \overset{def}{=} \frac{\lambda(t)}{R_c} \tag{7.2}$$

It is important to understand that λ is the average crack length and that there will be cracks of many different lengths inside the volume. If counting the average crack length in elements of different sizes, the crack length is proportional to the size of the element for a given damage D. When the element size increases one simply find cracks of longer lengths (again for a given damage). The MTSB model is especially suited to implementation in hydrocodes since an element cell can be declared as failed when the average crack length λ reaches the cell dimension R_c.

It now only remains to specify the functional form of the fracture strain and then we are done. The simplest possible option would be to use a constant fracture strain. However, this would lead to the same fracture strain in compression and tension, which is not in agreement with the static tests. Instead we assume the fracture strain to be a linear function of pressure *p*. This is different from the JC model where the ratio p/σ_M is used. Also, dividing with the Mises stress gives numerical problems for pure compressive and tensile loading, and such a model is therefore not robust. Thus, we have for MTSB:

$$\varepsilon_f^{mod} = max(0, a + bp) \tag{7.3}$$

where *a* and *b* are material constants which must be determined from our uniaxial static tests.

Describing the behaviour of tungsten carbide during these tests with the MTSB model, the crack length λ grows according to Equation (7.1) until $\lambda = R_c$ when the material fractures, i.e. when $\varepsilon_p = \varepsilon_c$ (compression) or $\varepsilon_p = \varepsilon_t$ (tension).

By integrating Equation (7.1) for crack growth, we then obtain:

$$\textit{Uniaxial compression}: \qquad \int_0^{R_c} \frac{\dot{\lambda}(t)dt}{R_c} = 2\int_0^{\varepsilon_c} \frac{d\varepsilon_p}{a + bp(\varepsilon_p)}$$

$$\textit{Uniaxial tension}: \qquad \int_0^{R_c} \frac{\dot{\lambda}(t)dt}{R_c} = 2\int_0^{\varepsilon_t} \frac{d\varepsilon_p}{a + bp(\varepsilon_p)}$$

The left hand side is easily seen to be equal to one and R_c therefore drops out of the equations, as was to be expected. Substituting $p = \pm\frac{1}{3}Y(\varepsilon_p)$ on the right hand side then gives us two equations for the two unknown parameters *a* and *b* in the fracture strain expression.

If we had an analytical expression for *Y* (which would have been relatively easy to find from curvefitting), these equations could possibly be solved analytically (depending on whether the integral is solvable). In any case, they can be solved numerically for *a* and *b*. For our tungsten carbide an approximate numerical solution is given by:

$$a = \varepsilon_c - p_t\left(\frac{0.9\varepsilon_t - \varepsilon_c}{p_t - p_c}\right) = 0.858$$

$$b = \frac{0.9\varepsilon_t - \varepsilon_c}{p_t - p_c} = 27.8 / MPa$$

7.1.2 Relationship between microcracks and macroscopic properties

It now remains to find a relationship between microcracks and macroscopic properties. We start by assuming the same form for the yield stress as in Johnson-Cook, i.e. as a function of plastic strain, but dropping the strain rate and temperature factor. This obviously has the advantage that the yield curve can easily be derived from a static uniaxial test, unlike for Johnson-Holmquist, where obtaining material parameters is, as we saw, much more difficult. (This is of course not an argument that tungsten carbide actually can be described using such a model, but until proven otherwise, we follow the Occam's Razor principle and persevere with what is simple). For

simplicity we also assume that MTSB is passive, just as Johnson-Cook. Therefore we have for MTSB:

$$Y = \begin{cases} A + B\varepsilon^n & \lambda < R_c \\ 0 & \lambda = R_c \end{cases} \tag{7.4}$$

7.1.3 Dynamic effects

It was clear from the tests of the other fracture models that a correct dynamic behaviour is important in the description of tungsten carbide. Unfortunately, since we have performed no dynamic measurements, we have very little information to go on. However, in earlier experiments (15) tungsten carbide projectiles were shot into semi-infinite targets at velocities of around 950 m/s. In those cases large plastic flows without significant fractures were found. This indicates that there at least is a strong dynamic dependency in compression. We thus, as a null hypothesis, assume significant strain rate dependency in the compressive fracture strain only. It is then given by

$$\varepsilon_c = \varepsilon_c^0 + \alpha\, \dot{\varepsilon}_p \tag{7.5}$$

where ε_c^0 is the plastic strain at fracture during the uniaxial static compression test and α is the dynamic parameter. Again, since we have performed no dynamic tests, the value of α will be calibrated in the yaw simulations.

7.2 Modified Johnson-Cook model

To modify the JC-model, we simply remove the strain rate dependency through the two constants *C* and D_4. Instead we use the same strain rate function as in MTSB. Thus, the Modified JC-model is given by:

$$Y = \begin{cases} A + B\varepsilon_p^n & D < 1 \\ 0 & D = 1 \end{cases}$$

$$\dot{D}(t) = \frac{\dot{\varepsilon}_p(t)}{\varepsilon_f(t)}, \quad 0 \le D \le 1, D(t_0) = 0,$$

$$\varepsilon_f(t) = D_1 + D_2 Exp\left(-D_3 \frac{p(t)}{\sigma_M(t)}\right)$$

$$D_1 = 0 \qquad D_2 = \sqrt{(\varepsilon_c^0 + \alpha\dot{\varepsilon}_p)\varepsilon_t} \qquad D_3 = -\frac{3}{2}\ln\left(\frac{\varepsilon_c^0 + \alpha\dot{\varepsilon}_p}{\varepsilon_t}\right)$$

We are now ready to put the two new materials model to the test.

8 Yaw numerical simulations for Modified Johnson-Cook and MTSB

Here we present the numerical results from the yaw simulations for the two new material models, MTSB and Johnson-Cook. Obviously, neither of these models are standard in AUTODYN, so they were implemented through a user subroutine. As mentioned many times, no dynamic material tests have been performed, so experimental values for the dynamic constant α were not available for tungsten carbide. This parameter was therefore tuned in the MTSB simulations to approximately the lowest value which resulted in an intact nose. A value of $\alpha = 5 \cdot 10^{-3} ms$ was found and used both in the MTSB and Modified Johnson-Cook simulations.

8.1 MTSB

An initial crack length $\lambda_0 = 1.7 \cdot 10^{-3}$ mm was used for the MTSB crack growth model corresponding to the average grain size of the sintered tungsten carbide penetrator, which we believe roughly corresponds to the size of initial flaws. The results are shown in Figure 8.1.

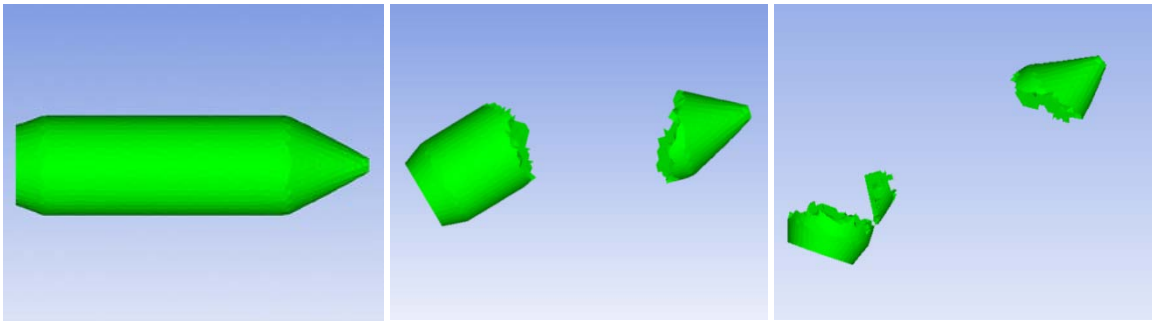

Figure 8.1 State of the tungsten carbide projectile after perforating a 5 mm RHA target at 0, 8 and 18 degrees yaw using the MTSB model with $\alpha = 5 \cdot 10^{-3} ms$

8.2 Modified Johnson-Cook

The Modified Johnson-Cook results are shown in Figure 8.2.

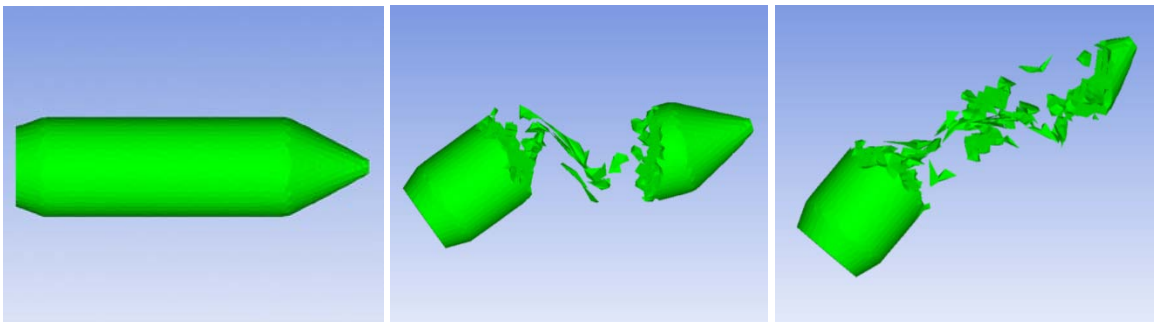

Figure 8.2 State of the tungsten carbide projectile after perforating a 5 mm RHA target at 0, 8 and 18 degrees yaw using the Modified Johnson-Cook model with $\alpha = 5 \cdot 10^{-3} ms$

8.3 Summary

The new results are in general a great improvement on the results given by the "old" models. The Modified Johnson-Cook and the MTSB model give quite similar results, despite being relatively different material models. The nose seems to be more intact for 18 degrees yaw using the MTSB model, but increasing the value of the dynamic parameter α would have given similar results for Modified Johnson-Cook. In total, the results are in pretty good agreement for the two new models. So these two models look the most promising so far, passing both the static material tests and experimental perforation yaw tests.

Table 8.1 presents an updated list of the material models we have tried for tungsten carbide. Note that "falsified" only means "falsified for tungsten carbide". Both JC and JH have been shown to work for a large number of other materials. There is thus nothing inherently wrong with these models, but they are just not applicable to tungsten carbide.

Table 8.1 Material models tried for tungsten carbide

	Simple	Johnson-Cook	Johnson-Holmquist II	Modified Johnson-Cook	MTSB crack growth
Description					
Type	Passive	Passive	Active	Passive	Passive
Fracture parameter	Damage	Damage	Damage	Damage	Crack length
Dynamic effects	None	Yield function, fracture strain	Yield function	Compressive failure strain	Compressive failure strain
Stress or strain based	Stress and strain	Strain	Stress	Strain	Strain
Performance					
Static test	Ok	Ok	Failed	Ok	Ok
Yaw test	Failed	Failed	Ok	Ok	Ok
Status	Falsified	Falsified	Falsified	Candidate	Candidate

9 Oblique impact perforation experiments

In previous chapters we saw that impact with yaw could lead to fracture of the tungsten carbide projectile. None of the conventional material models (Johnson-Cook and Johnson-Holmquist) were able to describe both this process and the static material tests. However, two new material models (MTSB and Modified Johnson-Cook) were seen to provide good results in both cases. Until proven wrong, these new models are therefore candidates for being a correct description of tungsten carbide.

In this chapter we will describe additional experiments that were performed and then numerically simulated. The idea was to test the MTSB and Modified Johnson-Cook models further in order to either falsify them as a description of tungsten carbide or obtain greater confidence in them.

In the new experiments we tried oblique impact (instead of yawed impact) against a variety of different steel targets. The test setup is shown in Figure 9.1. Projectiles were fired from the same standard ballistic test gun as in the yaw experiments. An impact velocity of 890 m/s was attempted and velocity was measured just before the projectile hit the steel target plate. The target plate was adjusted relative to the line of flight of the projectile, giving the different angles of impact. The impact angles were chosen to be 0°, 8° and 18°, hence corresponding to the magnitude of the yaw angles in the previous experiments.

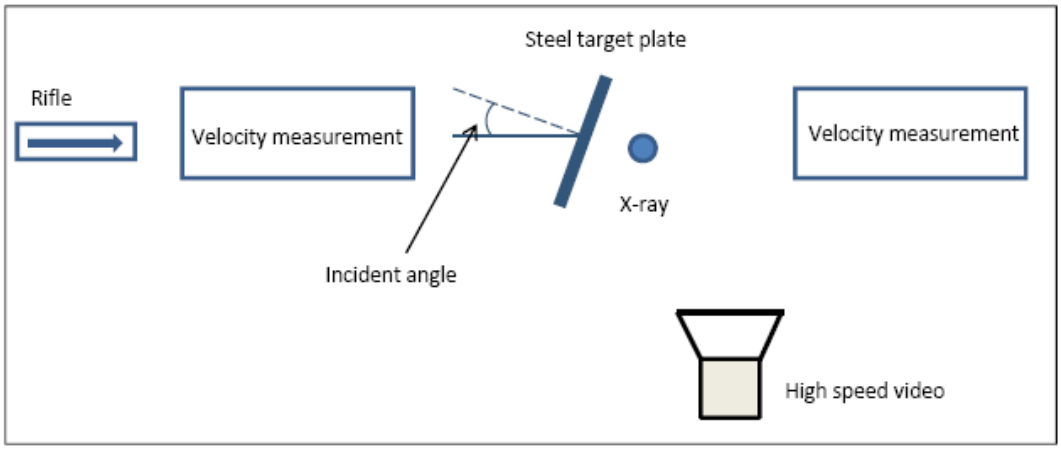

Figure 9.1 Experimental setup for the oblique impact tests.

Flash x-ray together with high speed camera were used to assess the fracturing behaviour of the projectiles. Velocity measurement after perforation was done for a small selection. Due to interference between the light gates in the velocity gauge and the flash x-ray, these assessment tools were however not used simultaneously. Yaw angle was not measured in these experiments., which therefore have an uncertainty of a few degrees yaw.

Experiments were carried out for three different types of 5 mm thick steel targets. The various types of steel are listed in Table 9.1 together with the measured reduction in projectile velocity after perforation at zero degrees impact.

Table 9.1 Steel types with corresponding velocity reduction after perforation at zero degrees

Steel type	Projectile velocity reduction (m/s)
Construction steel ST355	-78
RHA (same as in yaw experiments)	-115/-106
Armox 560T	-123

Flash X-ray pictures of the projectile after perforation are shown in Figure 9.2.

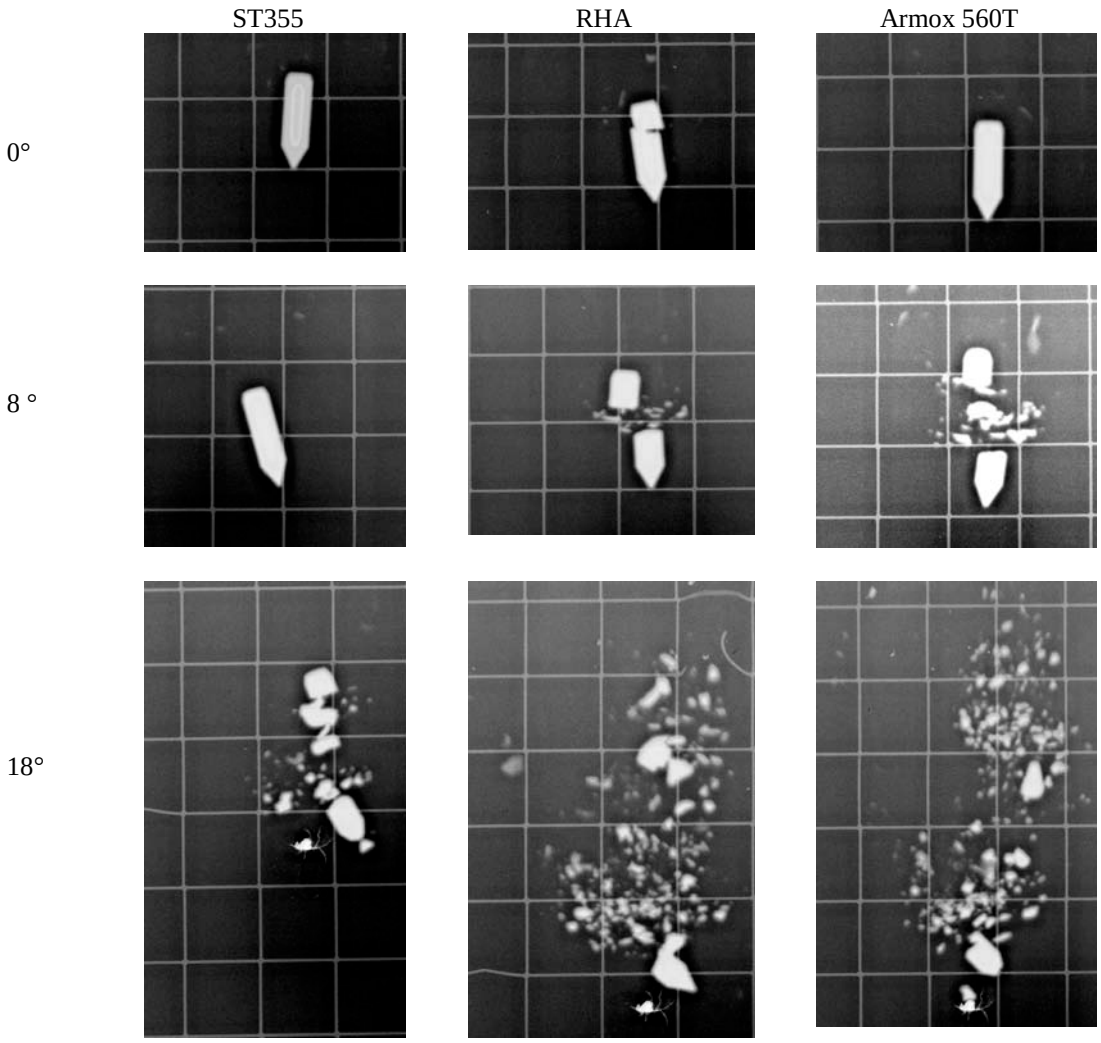

Figure 9.2 The tungsten carbide projectile after perforation of the different steel plates at different angles of impact.

We note that the projectile is unfractured against construction steel and Armox 560T for zero degrees, but has fractured slightly for RHA. The fracture in the RHA case is probably due to either a slightly higher (unwanted) yaw angle or the fact that this particular projectile was made of slightly weaker material. As we have noted before, there is some stochastic variation in the material properties for the different projectiles.

At 8 degrees oblique impact, the projectile remains unfractured in the ST355 case, but fractures into two larger and a few smaller fragments when shot at RHA and Armox 560T. For 18 degrees oblique impact, the projectile fractures for all three cases, and becomes quite pulverized except for the nose and rear part against the two harder steel types.

The MTSB and Modified JC-model gave good results for the fracture in the yaw experiments, but of course, we had the advantage of being able to tune the dynamic parameter α. It will therefore be interesting to see whether the models can replicate the oblique impact experiments described in this chapter without additional tuning of any parameters.

10 Numerical simulations of oblique impact experiments

Numerical simulations of the experiments were again performed in 3D using ANSYS AUTODYN v12.0. The same penetrator and target geometry as in the yaw experiments were used. The impact velocity was again chosen to be 890 m/s, corresponding roughly to the average experimental impact velocity.

The simulations were performed with the MTSB crack growth model and the Modified Johnson-Cook model. Exactly the same material parameters as in the yaw simulations were used and thus there was no additional tuning of the tungsten carbide parameters.

Static tests were performed on the three different steel types to determine the yield curve. The strain rate parameter of the steel was slightly tuned to increase the strength of steel to better match the simulated perforation velocity with the experiments. The steel models used in the simulations are given in Appendix C.

The exit velocities after perforating the steel target plate at zero degrees are shown in Table 10.1 together with the experimental values. The results are identical for MTSB and Modified JC since no fracturing takes place. We note that the ST355 seems to be slightly softer in the numerical simulations than in the experiments, but otherwise the agreement is good.

Table 10.1 Steel types with corresponding velocity reduction after perforation at zero degrees impact

Steel type	Experimental projectile velocity reduction (m/s)	Numerical projectile velocity reduction (m/s)
ST355	78	66
RHA	115/106	108
Armox 560T	123	124

We will now look at the final state of the projectile and compare with the x-ray photos in Figure 9.2.

10.1 Modified Johnson-Cook

The final states of the Modified JC-projectile after perforating the different targets at 0°, 8° and 18° obliquity are displayed in Figure 10.1. We see that the correspondence with experiments is good in many cases, but for 8 degrees the simulation do not predict fracture for RHA and Armox.

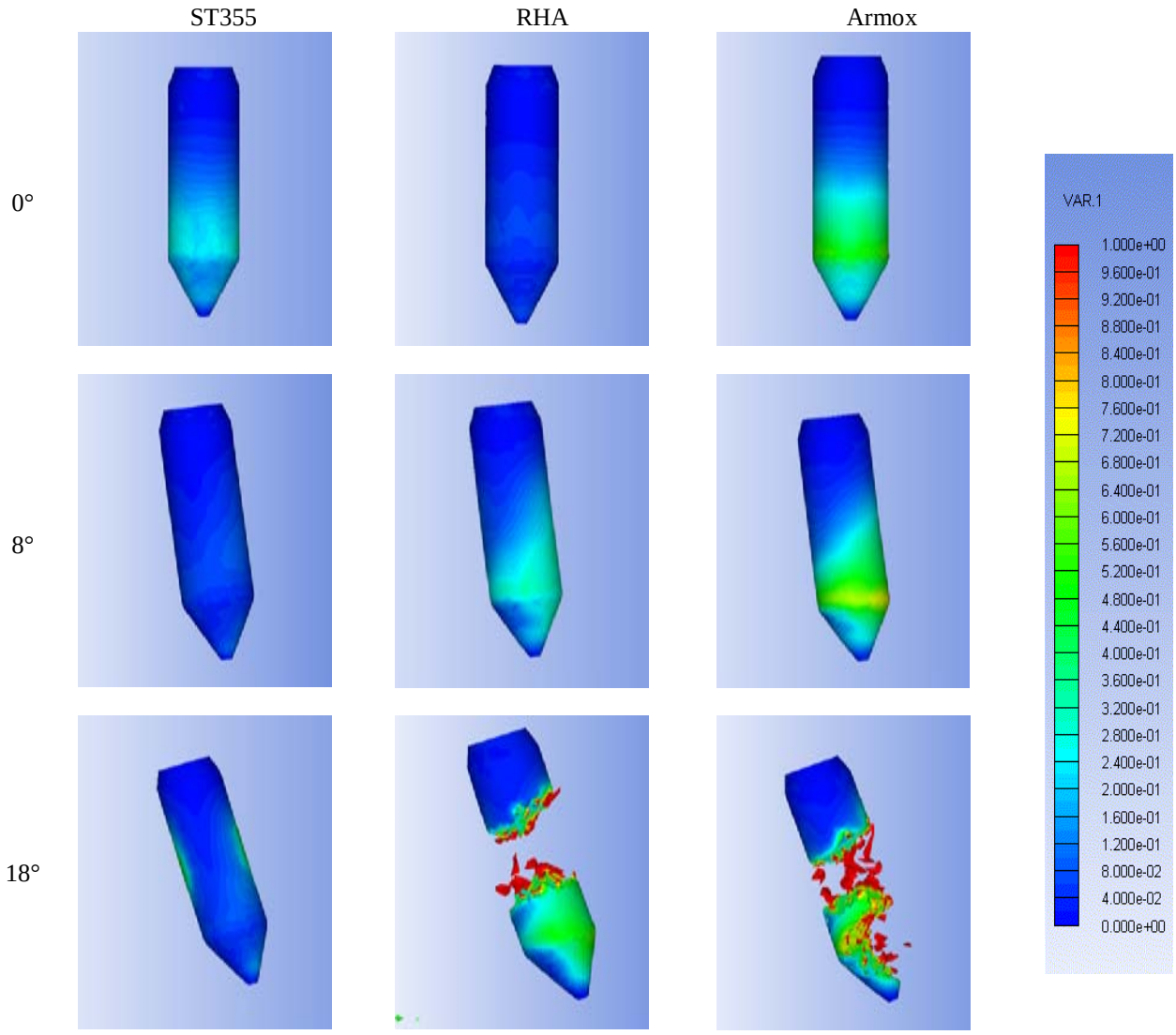

Figure 10.1 The damage state of the Modified Johnson-Cook tungsten projectile after perforating 5 mm steel targets at 0 degrees (left), 8 degrees (middle) and 18 degrees (right) oblique impact.

10.2 MTSB crack growth model

The results for different angles of oblique impact using the MTSB tungsten carbide model against the various steel plates are shown in Figure 10.2. The projectile with MTSB is quite similar to what was seen for Modified JC, although MTSB also correctly predicts fracture for 18 degrees against the ST355.

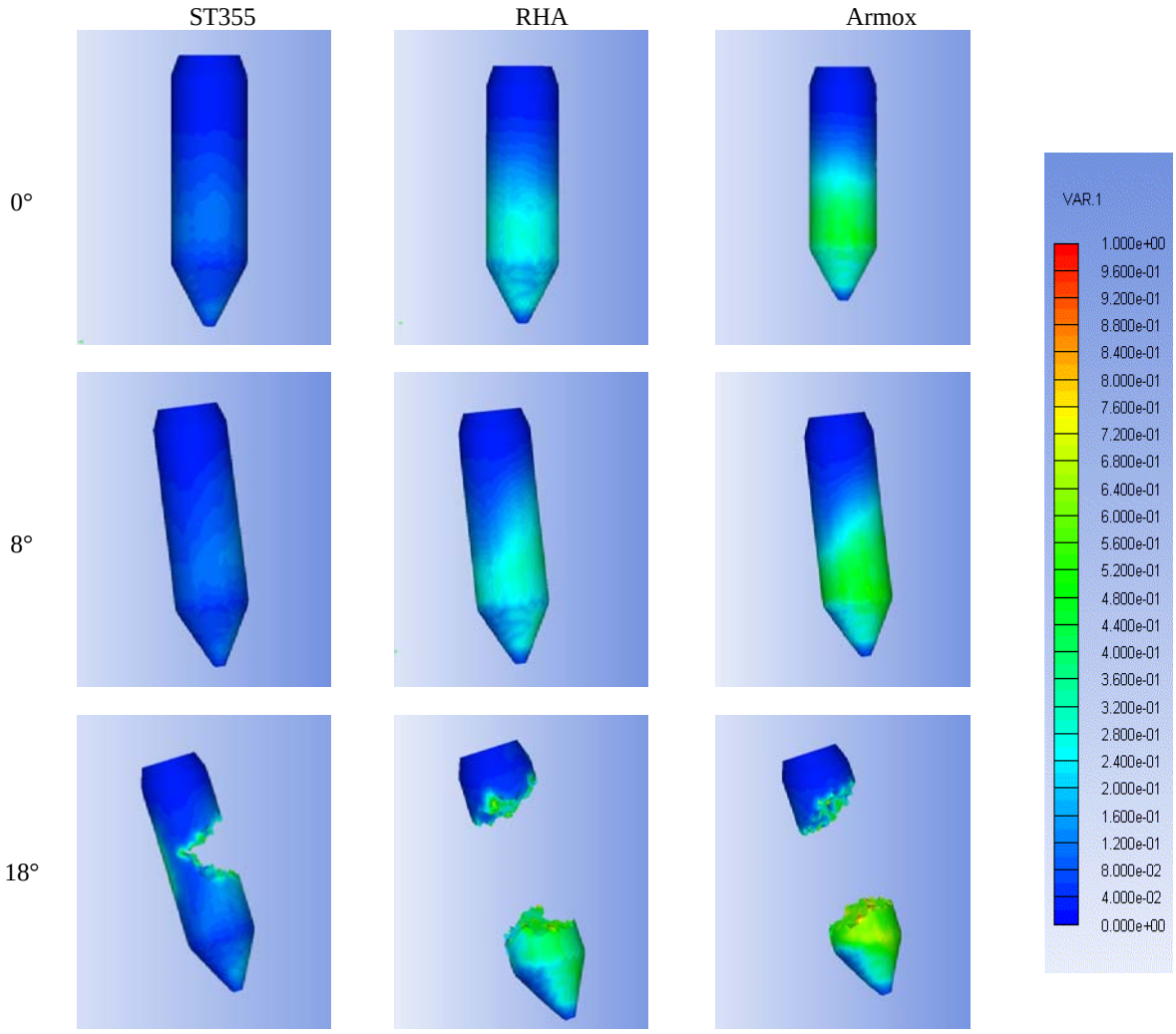

Figure 10.2 The damage state of the MTSB tungsten projectile after perforating 5 mm steel targets at 0 degrees (left), 8 degrees (middle) and 18 degrees (right) oblique impact.

Typically for both material models, there is generally quite good agreement with the experimental results, although the projectile seems to be a little bit less likely to fracture in the simulations. Still, in most cases when the numerical simulations did not show fracture, we see that the crack growth had advanced significantly bringing the projectile close to fracture.

However, the experimental fracture may have been due to (unwanted) yaw, since there is an uncertainty of a few degrees for the yaw. To test this, the 8 degrees simulations were rerun with added yaw for 3 degrees. Then fracture was obtained with the MTSB model for these cases as well, and thus we have perfect agreement with experiments. The Modified JC-model requires a little more added yaw to obtain fracture. However, note that the dynamic parameter in Modified JC was calibrated to the MTSB-model. A different calibration may have given even better results with Modified JC. In total, though, it seems fair to say that the MTSB model clearly passed the oblique impact test and possibly the Modified JC as well.

10.3 Material model summary

Table 10.1 presents an updated list of the material models we have tried and their performance.

Table 10.1 Tungsten carbide material models

	Simple	Johnson-Cook	Johnson-Holmquist II	Modified Johnson-Cook	MTSB crack growth
Description					
Type	Passive	Passive	Active	Passive	Passive
Fracture parameter	Damage	Damage	Damage	Damage	Crack length
Dynamic effects	None	Yield function, fracture strain	Yield function	Compressive failure strain	Compressive failure strain
Stress or strain based	Stress and strain	Strain	Stress	Strain	Strain
Performance					
Static test	Ok	Ok	Failed	Ok	Ok
Yaw test	Failed	Failed	Ok	Ok	Ok
Oblique test				Ok(?)	Ok
Status	Falsified	Falsified	Falsified	Candidate	Candidate

11 Summary

The topic of this report has been the development of a material model for semi-brittle materials like tungsten carbide. While the fracturing of brittle and ductile materials have been well described in the literature, nobody has until now created a material model for a hybrid with both ductile and brittle properties.

We started out by performing yawed perforation experiments with tungsten carbide projectiles to study their fragmentation properties. Then we tried to model these experiments numerically, using state-of-the-art material models like Johnson-Cook and Johnson-Holmquist. We discovered that these model seemed unable to model tungsten carbide.

Johnson-Holmquist failed already at the first hurdle, as it was not consistent with the strain hardening seen during the uniaxial material tests. Johnson-Cook was in perfect agreement with the static tests, but could not model the yaw experiments. It either incorrectly predicted fracturing of the nose, or if the dynamic parameter was tuned to "save the nose", the projectile body was not brittle enough.

To improve on this situation, two new models were developed. The MTSB crack growth model was developed from scratch, based on microcrack theory, whereas the dynamic dependency in the JC-model was changed to give us a Modified Johnson-Cook model. Both these new models were seen to agree both with the static tests and the yaw experiments.

To test the new models further, oblique impact experiments were performed against three different steel targets. Both models were able to replicate the numerical results without additional tuning of any parameters, increasing our confidence in them. The MTSB model was seen to perform particularly well.

In total, two new candidates for tungsten carbide material models have been developed. They have been tested in various experiments and so far good agreement has been found. Obviously, it will never be possible to prove that either of these are correct descriptions of tungsten carbide, but our experiences so far seem to indicate that they are at least valid in a large range of situations.

The results presented in this report represent a significant step forward in the understanding of semi-brittle materials. It should be mentioned that our findings have already been presented at two international conferences (International Symposium on Ballistics (23) and European Survivability Workshop (24)). Further, the implementation of the new fracture models in AUTODYN means that we have a powerful numerical tool for performing simulations involving such materials.

References

(1) Frøyland Ø, Moxnes J F: Mechanical studies of wolfram carbide, FFI/Rapport 2004/03860

(2) Frøyland Ø, Moxnes J F: Tensile tests of Wolfram carbide hard cores, FFI/RAPPORT-2006/03865

(3) Frøyland Ø, Moxnes J F: Microscopic studies of wolfram carbide after fracturing. FFI/Rapport-2004/01883

(4) Moxnes J F, Frøyland Ø: Hardness tests used to establish constitutive models. FFI/Rapport-2006/02802

(5) Moxnes J F, Frøyland Ø: Simple compression studies of wolfram carbide, FFI/RAPPORT-2006/01922

(6) Teland J A: A review of analytical penetration mechanics, FFI/RAPPORT-99/01264

(7) Teland J A, Svinsås E: Everything you wanted to know about material testing but were afraid to ask, FFI/RAPPORT-2003/00155

(8) Araki M, Kikuchi H, Nishida E, Ueno N, Yoneda J: Shock compaction of tungsten carbide, Rev. High Pressure sci. Technol. v. 7, pp. 915-917, 1998

(9) Dandekar D P, Grady D E: Shock equation of state and dynamic strength of tungsten carbide, Shock Compression of Condensed Matter, American Institute of Physics, pp. 783-786, 2001

(10) Johnson G R, Cook WH: Fracture Characteristics of Three Metals Subjected to Various Strains, Strain Rates, Temperatures and Pressures, J. Eng. Fracture Mechanics, Vol 21, Issue 1, pp. 31-48, 1985

(11) Holmquist T J, Johnson G R, Gooch W A, Modeling the 14.5 mm BS41 projectile for ballistic impact computations, Comp. Ballistics, Cordoba, Spain, May 18-20, 2005.

(12) Johnson G R, Holmquist T J: A Computational Constitutive Model for Brittle Materials Subjected to Large Strains, Shock-Wave and High strain-rate Phenomena in Materials, Marcel Dekker Inc. New York, pp 1075-1081, 1992

(13) Johnson G R, Holmquist T J: An improved computational Constitutive model for Brittle materials, High Pressure Science and Technology, AIP press, 1994.

(14) Taylor E A, Tsembelis K, Hayhurst C J, Kay L, Burchell M J, Hydrocode modelling of hypervelocity impact on brittle materials: depth of penetration and conchoidal diameter. Int. J. Impact. Eng., 23, pp. 895-904, 1999

(15) www.ansys.com

(16) Friis E, Moxnes J F: Penetration of Tungsten Carbide into Steel Targets, 21th International Symposium on Ballistics, Adelaine, Australia, April 19-23, 2004

(17) Friis E, Frøyland Ø, Moxnes J.F: Experimental and numerical study of the penetration of tungsten carbide into steel targets during high rates of strain, 22th International Symposium on Ballistics, Vancouver, Canada, 14-23, November, 2005

(18) Zhang Y O, Hao H: Dynamic fracture in brittle solids at high rates of loading . Transactions of the ASME v. 70, pp. 454-457, May 2003

(19) Holmquist T J, Johnson G J, Grady D E,Lopain C M, Hertel Jr: High Strain Rate Properties and Constitutive Modeling of Glas, 15th International Symposium on Ballistics, Jerusalem, Israel, 21-24, May, 1995

(20) Holmquist T, Johnson G J: Response of Silicon Carbide to high Velocity Impact", J. Appl. Phys., 91,(9), pp. 5858-5866, 2002

(21) Johnson G J, Holmquist T: Response of Boron Carbide Subjected to Large Strains, High Strain Rates, and High Pressures, J. Appl. Phys.85,(12),pp. 8060-8073, 1999

(22) Tuler F R, Butcher B M: A criterion for the time dependence of dynamic fracture. Int. J. Fracture Mechanics, vol 4, no 4, pp. 431-437, 1968

(23) Moxnes J F, Teland J A, Skriudalen S, Bergsrud S M: Experimental and numerical study of the penetration of tungsten carbide projectiles into steel targets, Proceedings of the 25th International Symposium on Ballistics, Beijing, China, May 17-21, 2010

(24) Moxnes J F, Teland J A, Skriudalen S, Bergsrud S M, Vulnerability modelling of structures perforated by tungsten carbide projectiles, Proceedings of the 5th European Survivability Workshop, Ålesund, Norway, June 8-10, 2010

Appendix A RHA plate hardness measurements

Figure A.1 Hardness measurement for steel plate used for shots 1-16 in the yaw experiments. Both sides and the edge were measured.

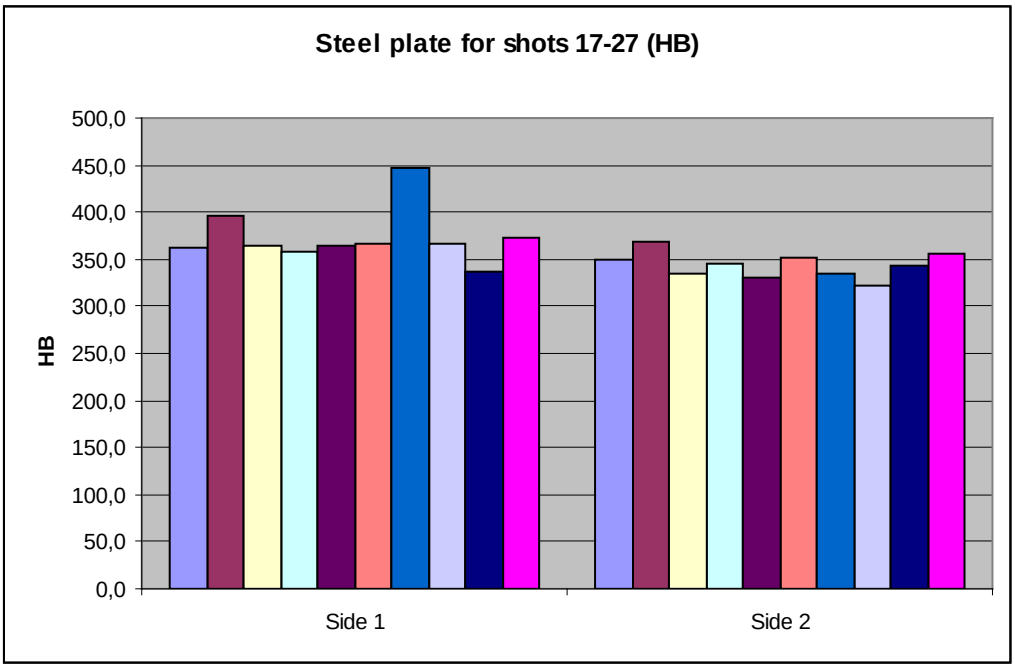

Figure A.2 Hardness measurement for steel plate used in shots 17-27 in the yaw experiments. Both sides were measured.

Appendix B Tungsten carbide material models

Equation of State	**Linear**
Reference density	1.45600E+01 (g/cm3)
Bulk Modulus	3.48000E+08 (kPa)
Strength model	**User Strength #1**
Shear Modulus	2.38980E+08 (kPa)
Eff. plastic strain #1	0.00000E+00 (none)
Eff. plastic strain #2	2.63000E-04 (none)
Eff. plastic strain #3	9.73640E-04 (none)
Eff. plastic strain #4	2.10700E-03 (none)
Eff. plastic strain #5	3.57400E-03 (none)
Eff. plastic strain #6	5.28700E-03 (none)
Eff. plastic strain #7	7.17600E-03 (none)
Eff. plastic strain #8	9.19000E-03 (none)
Eff. plastic strain #9	1.12900E-02 (none)
Eff. plastic strain #10	1.34520E-02 (none)
Eff. plastic strain #11	1.42790E-02 (none)
Eff. plastic strain #12	1.00000E-01 (none)
Yield stress #1	4.19530E+05 (kPa)
Yield stress #2	1.69690E+06 (kPa)
Yield stress #3	2.67550E+06 (kPa)
Yield stress #4	3.37650E+06 (kPa)
Yield stress #5	3.85820E+06 (kPa)
Yield stress #6	4.17800E+06 (kPa)
Yield stress #7	4.38220E+06 (kPa)
Yield stress #8	4.50480E+06 (kPa)
Yield stress #9	4.57010E+06 (kPa)
Yield stress #10	4.59550E+06 (kPa)
Yield stress #11	4.59730E+06 (kPa)
Yield stress #12	4.59730E+06 (kPa)
Johnson-Cook failure model	

Damage Constant, D1	0.00000E+00 (none)
Damage Constant, D2	1.07200E-02 (none)
Damage Constant, D3	-1.66900E+00 (none)
Damage Constant, D4	0.00000E+00 (none)
Damage Constant, D5	0.00000E+00 (none)
Johnson-Holmquist strength model	
Shear Modulus	2.19020E+08 (kPa)
Model Type	Continuous (JH2)
Hugoniot Elastic Limit	6.56600E+06 (kPa)
Intact Strength Constant A	9.89900E-01 (none)
Intact Strength Exponent N	3.22000E-02 (none)
Strain Rate Constant C	0.00000E+00 (none)
Fractured Strength Constant B	6.70000E-01 (none)
Fractured Strength Exponent M	3.22000E-02 (none)
Max. Fracture Strength Ratio	1.00000E+03 (none)
Johnson-Holmquist failure model	
Hydro Tensile Limit (Low/High)	-1.3E+06 / -4.0E+06 (kPa)
Model Type	Continuous (JH2)
Damage Constant, D1	5.00000E-03 (none)
Damage Constant, D2	1.00000E+00 (none)
Bulking Constant, Beta	0.00000E+00 (none)
Damage Type	Gradual (JH2)
Tensile Failure	Hydro (Pmin)
Modified Johnson-Cook failure model	
D1	1.00000E-03 (none)
Compressive fracture limit strain rate constant	5.00000E-03 (none)
Static compressive fracture plastic strain	9.40000E-03 (none)
Tensile fracture plastic strain	3.50000E-03 (none)
MTSB crack growth model	
Compressive strength	4.53000E+06 (kPa)
Tensile strength	3.85000E+06 (kPa)

Compressive fracture plastic strain	9.40000E-03 (none)
Tensile fracture plastic strain	3.50000E-03 (none)
Lambda0	1.70000E-03 (mm)
Compressive fracture limit strain rate constant	5.00000E-03 (/ms)

Appendix C Material models for steel plate targets

Armox570T

Equation of State	**Linear**
Reference density	7.85000E+00 (g/cm3)
Bulk Modulus	1.71670E+08 (kPa)
Strength	**Johnson Cook**
Shear Modulus	7.92300E+07 (kPa)
Yield Stress	2.03000E+06 (kPa)
Hardening Constant	5.68000E+05 (kPa)
Hardening Exponent	1.00000E+00 (none)
Strain Rate Constant	3.00000E-02 (none)
Thermal Softening Exponent	1.00000E+00 (none)
Melting Temperature	1.80000E+03 (K)
Ref. Strain Rate (/s)	1.00000E+00 (none)
Strain Rate Correction	1st Order
Failure	**Plastic Strain**
Plastic Strain	9.20000E-01 (none)
Stochastic failure	No

RHA

Equation of State	**Linear**
Reference density	7.90000E+00 (g/cm3)
Bulk Modulus	1.71670E+08 (kPa)
Strength	**Johnson Cook**
Shear Modulus	7.92300E+07 (kPa)

Yield Stress	1.10000E+06 (kPa)
Hardening Constant	4.38000E+05 (kPa)
Hardening Exponent	2.50000E-01 (none)
Strain Rate Constant	5.00000E-02 (none)
Thermal Softening Exponent	0.00000E+00 (none)
Melting Temperature	0.00000E+00 (K)
Ref. Strain Rate (/s)	1.00000E+00 (none)
Strain Rate Correction	1st Order
Failure	**None**

Construction steel

Equation of State	**Linear**
Reference density	7.85000E+00 (g/cm3)
Bulk Modulus	1.96070E+08 (kPa)
Strength	**Johnson Cook**
Shear Modulus	7.51880E+07 (kPa)
Yield Stress	4.09000E+05 (kPa)
Hardening Constant	8.07000E+05 (kPa)
Hardening Exponent	7.30000E-01 (none)
Strain Rate Constant	5.00000E-02 (none)
Thermal Softening Exponent	1.00000E+00 (none)
Melting Temperature	1.80000E+03 (K)
Ref. Strain Rate (/s)	1.00000E+00 (none)
Strain Rate Correction	1st Order
Failure	**Plastic Strain**
Plastic Strain	9.20000E-01 (none)